C-terminus induced asymmetry within a Rad52 homodecamer dictates single-position Rad51 nucleation in homologous recombination

Jaigeeth Deveryshetty[1,§], Rahul Chadda[1,§], Jenna Mattice[2], Simrithaa Karunakaran[1], Michael J. Rau[3], Katherine Basore[3] Nilisha Pokhrel[4], Noah Englander[1], James A.J. Fitzpatrick[3], Brian Bothner[2] and Edwin Antony[1,*]

[1]Department of Biochemistry and Molecular Biology, Saint Louis University School of Medicine, St. Louis, MO

[2]Department of Chemistry and Biochemistry, Montana State University, Bozeman, MT

[3]Center for Cellular Imaging, Washington University in St. Louis School of Medicine, St. Louis, MO

[4]Department of Biological Sciences, Marquette University, Milwaukee, WI (Present address: Laronde Bio, Cambridge, MA, USA)

*Address Correspondence to: Dr. Edwin Antony, Department of Biochemistry and Molecular Biology, St. Louis, MO 63104. Ph: (314) 977 9257. Email: edwin.antony@health.slu.edu

§Authors contributed equally to this study.

Abstract

Homologous recombination (HR) is a pathway for the accurate repair of double-stranded DNA breaks, which are resected to yield single-strand DNA (ssDNA). Rad52 promotes HR by facilitating formation of Rad51 nucleoprotein filaments on ssDNA. Using single-particle cryo-electron microscopy, we show that Rad52 functions as a homodecamer. The N-terminal half of Rad52 is a well-ordered ring, while the C-terminal half is disordered. An intrinsic asymmetry within Rad52 is observed, where one or a few of the C-terminal halves interacts with the ordered N-terminal ring. Within the C-terminal half, we define two conserved charged patches that harbor the Rad51 and RPA interacting motifs. Interactions between these two charged patches promote asymmetry and regulate a two-stage ssDNA binding mechanism. Interestingly, the intrinsic asymmetry allosterically drives Rad51 binding to a single position on the Rad52 ring. We propose a Rad52 catalyzed single-position nucleation model for the formation of pre-synaptic Rad51 filaments in HR.

Introduction

Homologous recombination (HR) protects genomic integrity by repairing double-stranded breaks (DSBs).[1-3] Mutations to genes that encode for HR-related proteins are implicated in a plethora of human cancers and genetic disorders.[4,5] For accurate repair through HR, information from the undamaged sister allele is used as a template. In *Saccharomyces cerevisiae*, HR progresses through a series of defined steps beginning with resection, where the DSB is processed by the Mre11-Rad50-Nbs1 (MRN) complex yielding 3′ ssDNA overhangs.[1] The transiently exposed ssDNA is coated by the high-affinity ssDNA binding protein Replication Protein A (RPA)[6,7] which then recruits the Mec1-Ddc2 DNA-damage-sensing kinase to regulate downstream events in HR.[8,9]

Rad51, the recombinase, catalyzes identification and pairing of the homologous sequence in the undamaged allele. Rad51 forms a helical filament on ssDNA with defined ATP-driven nucleation and filament growth processes.[10,11] Formation of the Rad51 filament on RPA-coated ssDNA occurs during the pre-synaptic phase of HR. Since Rad51 binds to ssDNA with lower affinity ($K_D \sim 10^{-6}$ M) compared to RPA ($K_D < 10^{-10}$ M), mediator proteins are required to overcome the thermodynamic barrier to facilitate ssDNA handoff. Pro-HR mediators function to promote formation of Rad51 filaments whereas anti-HR mediators facilitate Rad51 disassembly.[10] In yeast, Rad52 is the sole pro-HR mediator. In mammals, Rad52 and Brca2 play overlapping roles in promoting Rad51 filament formation.[12,13] Deletion of *Rad52* in *S. cerevisiae* has severe defects in various recombination processes including Rad51-dependent allelic recombination and Rad51-independent single-strand annealing.[3,14-18]

In terms of the mechanism of action, yeast and human Rad52 have been considered to function as a heptameric rings.[19-22] However, structural studies of the C-terminal truncated human Rad52 show that the complex is an undecamer.[23,24] Thus, the functional stoichiometry of Rad52 in solution is uncertain. Both DNA binding and protein-protein interactions are integral to the recombinogenic functions of Rad52. When promoting Rad51 filament formation, Rad52 requires binding to ssDNA and substrates with a 3′ overhang. During strand annealing, Rad52 must simultaneously bind to two strands of ssDNA or one ssDNA and another dsDNA fragment. A new function for Rad52 in RNA-templated DNA repair was recently uncovered[25,26] that would require simultaneous binding to both DNA and RNA fragments.[27] Each Rad52 subunit is composed of an ordered N-terminal and disordered C-terminal half (Fig. 1a). The primary DNA binding activity

and the oligomerization regions are thought to be harbored in the N-terminal half[28] whereas Rad51 and RPA binding motifs reside in the disordered C-terminal half of Rad52.[29-34] A weaker DNA binding site has also been identified in the C-terminal region.[35,36] Two crystal structures of the N-terminal half of human Rad52 (residues 1-212) bound to ssDNA were recently solved.[37] An outer and inner DNA binding site in the ordered N-terminal half coordinates DNA binding in Rad52.[20,38,39]

Physical interactions between Rad52 and Rad51-RPA are essential for the mediator functions in HR, and both binding sites reside in the disordered C-terminal half of Rad52.[29-34] The C-terminus also promotes phase separation of Rad52 into liquid droplets and cluster DNA damage sites.[40] In addition to the above mentioned roles, Rad52 regulates the extent of DNA resection during HR by regulating the Rqh1 helicase in fission yeast.[41] Furthermore, Rad52 functions in other processes such as regulating retrotransposition,[42] CRISPR-Cas9 genome editing,[43] and IgD class-switch recombination.[44] Given the emerging multifaceted functions of Rad52, knowledge of it functions and mechanism of action is critical.

We show that *S. cerevisiae* Rad52 functions as a homodecamer with each subunit possessing an ordered N-terminal and disordered C-terminal half. Upon ssDNA binding, extensive conformational changes are observed in both the ordered N-terminal and disordered C-terminal halves of Rad52. More interestingly, we find an intrinsic asymmetry in Rad52 imparted by the C-terminal half. One, or a small subset of the C-termini interacts with the N-terminal ring and dictates ssDNA wrapping and diffusion properties. The allostery also dictates Rad51 binding to a single position in the Rad52 ring and guides Rad51 filament formation. Furthermore, interactions between Rad51 and N-terminal half are observed. Our findings reveal how the ordered decameric N-terminal ring and the disordered C-terminal region cooperate to perform the mediator role of Rad52 to faciliate Rad51 nucleation during HR.

Results

Saccharomyces cerevisiae Rad52 functions as a homodecamer

Yeast and human Rad52 are canonically considered to function as heptamers based on negative-stain transmission electron microscopy and analytical ultracentrifugation (AUC) analysis.[19-22] However, crystal structures of the N-terminal half of human Rad52 revealed an undecamer both in the absence or presence of ssDNA[22,23], with ssDNA encircling the ring in a uniform manner.[23,24,37] Thus, to establish the functional stoichiometry, we performed single-

particle cryo-EM analysis of full-length *S. cerevisiae* Rad52. Recombinantly overproduced and purified Rad52 is predominantly a single species in both mass photometry (MP) and analytical ultracentrifugation sedimentation velocity (AUC^{SV}) analyses over a range of protein concentrations tested (Fig. 1B and Supplementary Fig. 1). A small fraction (~5-10%) of a higher order species is observed and corresponds to double the mass of the major peak. The predicted mass of one Rad52 subunit is 52.4 kDa and measurements from MP and AUC yield molecular weights of ~500 kDa (~10 monomers) and ~1000 kDa (~19-20 monomers) for the two species, respectively (Supplementary Tables 1 & 2). These data suggest that yeast Rad52 functions as a homodecamer in solution.

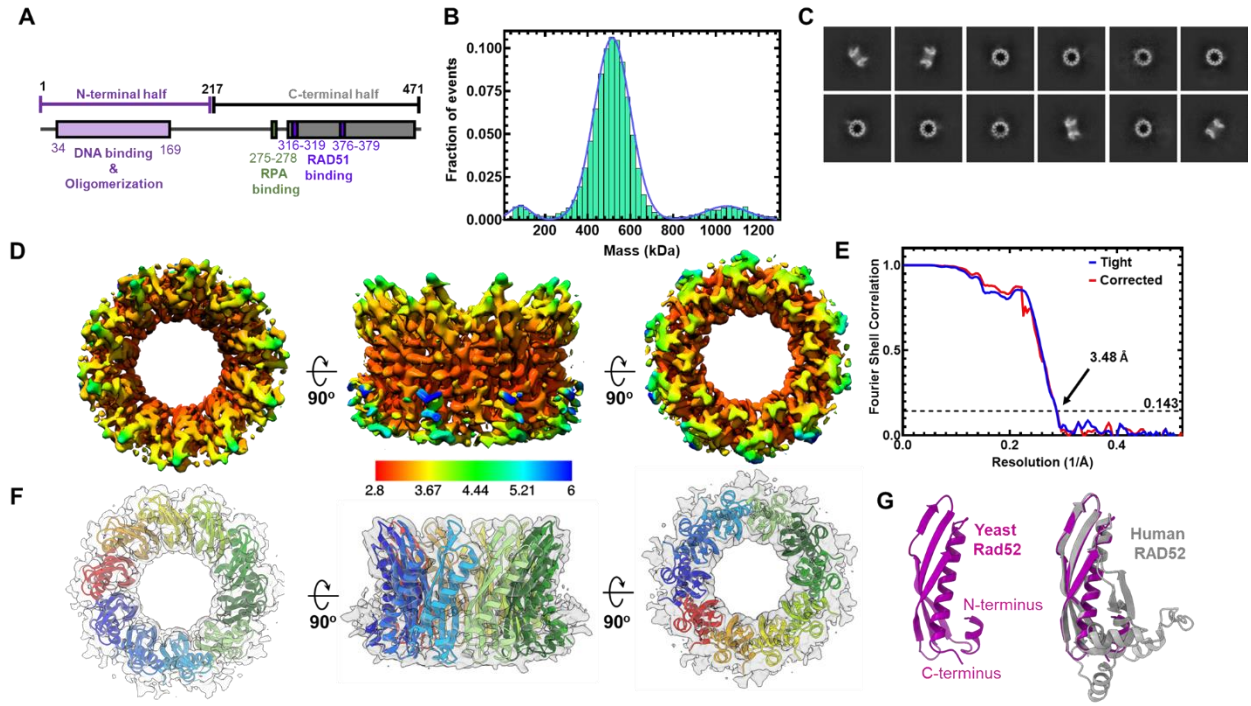

Figure 1. *S. cerevisiae* Rad52 functions as a homodecamer. A) Schematic representation of a yeast Rad52 subunit depicts N- and C-terminal regions that promote DNA binding, oligomerization, & protein-protein interactions. **B)** Mass photometry analysis predominantly shows a single Rad52 species. The major species (>85%) shows a mass of 498.4±23.8 kDa. A minor 991.8± 75.34 kDa species (~8-12%) is observed along with a small fraction of free monomers (72.9±13.9 kDa). **C)** Representative 2D classes of full-length yeast Rad52 observed in Cryo-EM analysis and used for determination of the structure. **D)** Color coded depiction of the local resolution mapped on to the Rad52 Cryo-EM map. **E)** Gold Standard Fourier shell correlation (FSC) curves calculated using Cryosparc. **F)** *De novo* built atomic model of Rad52 overlaid on the Cryo-EM map. **G)** Atomic model of a Rad52 subunit (magenta) aligned with the crystal structure of human RAD52 (grey; PDB 1KN0) using Chimera with Root Mean Square Deviation (RMSD) of 0.849 Å for Cα atoms of 87 amino acid pairs.

Cryo-EM structure of full-length S. cerevisiae Rad52

2D classification of Rad52 single particles in cryo-EM analysis confirmed that yeast Rad52 is a homodecameric ring (Fig. 1C & Supplementary Fig. 2), and no undecamers were observed. 3D reconstruction and subsequent refinement revealed strong density for the N-terminal half (Supplementary Fig. 3). However, only partial density was observed for the C-terminal half, which is consistent with the disordered nature. The final cryo-EM map reconstruction reached an average resolution of 3.5Å with local resolution ranging from 2.9 – 6Å (Figs. 1D-F & Supplementary Table 3). Using the refined map, a *de novo* model was built for the N-terminal region encompassing amino acids 55-143. This region of yeast Rad52 is structurally similar to human Rad52 (41% sequence identity)[24] with a RMSD of 0.849Å for Cα atoms of 87 amino acid pairs (Fig. 1G and Supplementary Fig. 4). We note two key differences between the yeast and human Rad52 structures[23,24]: In terms of stoichiometry, human Rad52 is an undecamer[23,24,37] whereas yeast Rad52 is a decamer. The petal-like extensions observed around the periphery of the ring structure of human Rad52 are dynamic in yeast Rad52 (Fig. 1G and Supplementary Fig. 4). These differences could be intrinsic to the properties of the two proteins or because the crystal structures of human Rad52 were obtained with the truncated protein (residues 1-212) containing only the N-terminal half[23,24,37]. The overall charge distribution and the interfaces that coordinate oligomerization are conserved between the two proteins (Supplementary Fig. 4).

Rad52 displays biphasic ssDNA binding activity

Next, to investigate how the Rad52 decamer bound to ssDNA, we followed the change in intrinsic tryptophan (Trp) fluorescence (Figs. 2A & B). We used poly(dT) or $(dT)_{84}$ to determine the occluded site-size of Rad52 which is defined as the number of ssDNA nucleotides required to saturate all the potential binding sites on the protein. Two binding phases are observed with a high (K_D = 1.3x10^{-12} M) and relatively lower affinity (K_D = 28x10^{-9} M) site saturating at 55±3 nt and 158±3 nt per Rad52 decamer, respectively (Fig. 2A & B, Supplementary Fig. 5A & B). In the DNA-bound crystal structures of human Rad52[37], depending on the mutations introduced to promote crystallization, an inner binding site was observed where a 40nt ssDNA oligonucleotide wraps around the undecameric ring (~3.6 nt/subunit; Supplementary Fig. 6A)[37]. An outer binding site was also captured with 6 nt of ssDNA sandwiched between two Rad52 undecameric rings (Supplementary Fig. 6B)[37]. In comparison, our data reveals that for yeast Rad52 ~5.5 nt/subunit and ~15 nt/subunit are required to saturate the high and low affinity binding sites, respectively.

These data suggest that even though the Rad52 decamer contains one subunit less as compared to human Rad52 the high affinity binding site is larger: 5.5 nucleotides/subunit as compared to 3-4 nucleotides/subunit indicating that the ssDNA wrapping by yeast Rad52 may not be uniform as observed for human Rad52.

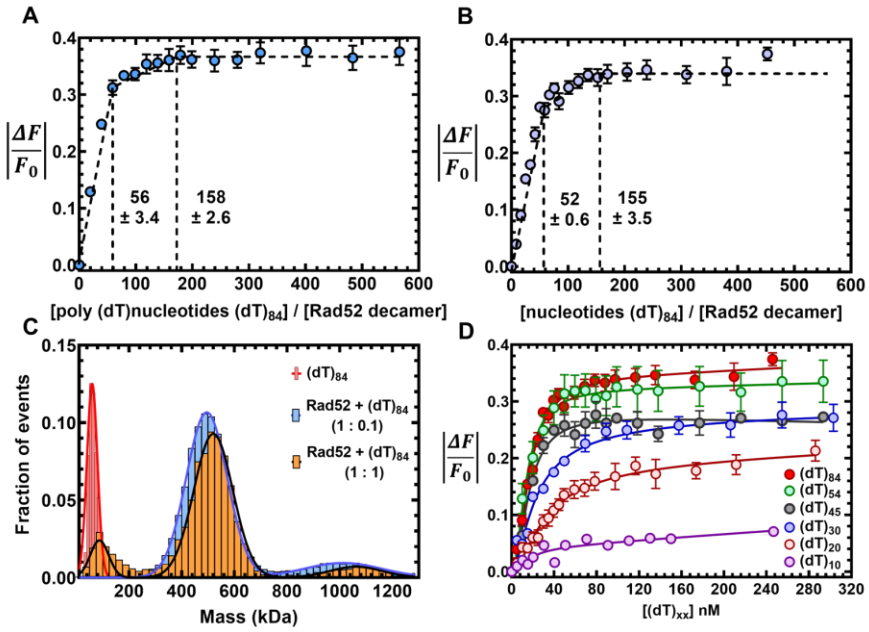

Figure 2. Rad52 non-uniformly binds to ssDNA using multiple binding. Tryptophan quenching experiments with **A)** poly(dT) or **B)** $(dT)_{84}$ reveal two ssDNA binding phases for Rad52 with sites sizes of 56±3 and 158±3, respectively. **C)** Mass photometry analysis of $(dT)_{84}$ or Rad52+$(dT)_{84}$ (1:0.1 or 1:1, $Rad52^{decamer}$:ssDNA) show that a single Rad52 homodecamer binds to $(dT)_{84}$. The small fraction of the higher order Rad52 molecules also bind to ssDNA and behave as a single DNA-bound complex. **D)** Tryptophan quenching of Rad52 as a function of ssDNA length shows that DNA lengths of >$(dT)_{45}$ are required to observe maximal signal quenching.

Another explanation for the data could be formation of higher order oligomers of Rad52 on ssDNA where more than one decameric ring could be envisioned to promote non-uniform binding. To investigate this possibility, we performed MP and AUC^{SV} analysis to ascertain the stoichiometry of yeast Rad52 decamers bound to ssDNA. When binding of Rad52 to short $(dT)_{45}$ or long ssDNA $(dT)_{97}$ is assessed, stoichiometric Rad52 decamer:DNA complexes are observed (Supplementary Fig. 5C). The minor fraction of two-Rad52 ring species also binds to equimolar amounts of ssDNA. On longer $(dT)_{97}$ or $(dT)_{84}$ ssDNA substrates, predominantly 1:1 complexes are observed even under conditions where a 10-fold excess of the Rad52 ring is present (Fig. 2C). Fluorescence anisotropy analysis reveals that Rad52 binding to ssDNA is highly specific (Supplementary Fig. 5B), and shows hallmarks of equilibrium complexation including saturation, high affinity (Supplementary Fig. 5A, B &C), and reversibility (Supplementary Fig. 5E).

Furthermore, the affinity for ssDNA interactions is dictated by the length of the ssDNA (Fig. 2D). Interestingly, Rad52 does not bind to dsDNA under these experimental conditions (Supplementary Fig. 5B). These data suggest that there are intrinsic differences in the ssDNA binding properties between the yeast and human Rad52 proteins. Next, we investigated whether the disordered C-terminal half of Rad52 contributes to non-uniform ssDNA binding.

Hydrogen-deuterium exchange mass-spectrometry (HDX-MS) reveals conformational changes in the C-terminus of Rad52 upon ssDNA binding.

While the C-terminal half of yeast Rad52 is disordered in our structure, interactions between this region and DNA have been captured.[36] Thus, to map the overall DNA binding driven conformational changes and to identify other potential DNA binding regions, we performed HDX-MS analysis of Rad52 in the absence or presence of ssDNA. Deuterium incorporation was quantified as a function of time for Rad52 and the Rad52-ssDNA [$(dT)_{97}$] complex. Peptide level deuterium uptake was compared between conditions (Supplementary Figs. 7-10). The difference in HDX between Rad52 and the Rad52-$(dT)_{97}$ complex (differential-HDX) were mapped onto an Alphafold model of the Rad52 monomer and shown as a heatmap (Fig. 3A). Regions colored blue and red depict increased and decreased differential-HDX, respectively. The Alphafold model aligns well with the cryoEM structure of the N-terminal half of Rad52 (Supplementary Fig. 10). Differential-HDX changes are observed in the N-terminal half upon DNA binding as well as inner, outer, and transition regions as expected based the homologous DNA binding regions in human Rad52 (Fig. 3B-D and Supplementary Figs. 7 & 8). Interestingly, a surprising number of peptides in the disordered C-terminal half also show changes in differential-HDX upon ssDNA binding (Fig. 3A, E-F, and Supplementary Figs. 9). One peptide in particular (residues 383-413) displays the largest HDX changes (Fig. 3E). A more detailed investigation of the MS data for this peptide shows an intriguing bimodal deuterium uptake pattern (Fig. 3F and Supplementary Fig. 11). In the absence of DNA, two populations of this peptide are observed that show low or high deuterium uptake. Calculation of the distribution based on ion intensity shows that ~70% of this peptide displays higher uptake (Fig. 3G). In the presence of ssDNA, a loss of the higher uptake population occurs. The data suggests an intrinsic asymmetry in the structural organization/accessibility of the C-terminal half (C-tails) of Rad52 where a small subset of the C-tails are protected from deuterium uptake.

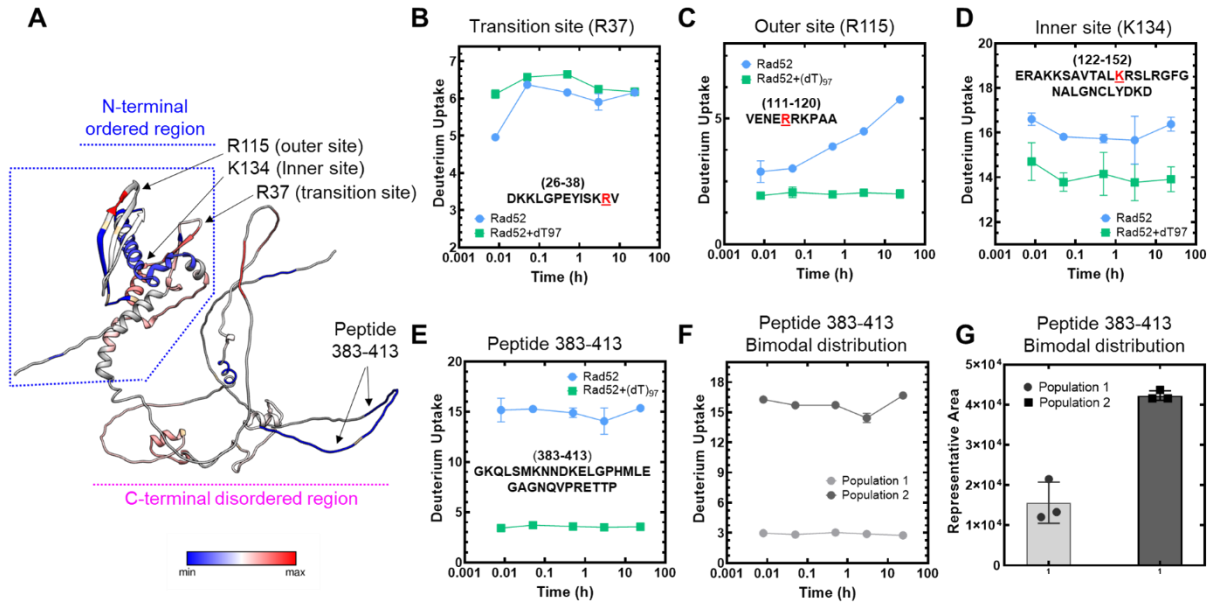

Figure 3. **Hydrogen-deuterium exchange mass-spectrometry reveals ssDNA driven changes in both the N- and C-terminal halves of Rad52. A)** Differential-HDX changes between Rad52 and the Rad52-$(dT)_{97}$ complex are projected on to the Alphafold predicted structure (AF-P06778-F1). DNA-induced HDX changes in the known DNA binding regions (inner, outer, and transition binding sites) are noted. Raw HDX data showing differences within peptides harboring **B)** Transition (R37), **C)** Outer (R115), and **D)** Inner (K134) ssDNA binding sites are shown with the key residues highlighted in red. **E)** Deuterium uptake profile for peptide 383-413 in the disordered C-terminal half shows a significant reduction in deuterium uptake upon ssDNA binding. **F)** and **G)** A bimodal distribution of deuterium uptake was observed in the Rad52 apo sample with least uptake by population 1 and high uptake by population 2. Population 1 represents only 30% of the total signal suggesting that not all subunits in Rad52 are uniform in structure or conformation.

Since there is a dichotomy in the behavior of C-tails, we reanalyzed our 2D classes from the Cryo-EM dataset to gain further insights into this asymmetry. Several 2D classes show the presence of extra bright density adjacent to one part of the decameric ring (Supplementary Fig. 12A). Unfortunately, detailed structural refinement was not possible since this is a disordered region. Low resolution 3D-volume calculations shows the extra density situated on the outer side of the ring closer to the N-terminal half of one side of the Rad52 decamer (Supplementary Fig. 12B). The data reveal an interesting structural feature where only a small subset of the C-tails interact with the decameric ring of Rad52.

Cross-linking mass spectrometry (XL-MS) analysis reveals interactions between the ordered N-terminal and disordered C-terminal halves of Rad52

To identify the regions of the disordered C-terminal half that interact with the ordered N-terminal region we performed XL-MS analysis of Rad52 with bis(sulfosuccinimidyl)suberate

(BS3).[45] The *N*-hydroxysulfosuccinimide (NHS) esters positioned at either end of the BS3 crosslinker are spaced 8-atoms apart and likely report on crosslinks with primary amines in Rad52 that are up to 12Å apart[46]. XL-MS analysis on Rad52 alone or in complex with ssDNA [$(dT)_{97}$] showed an extensive array of crosslinks (Fig. 4). ~38% and ~19% of the crosslinks are unique to the unbound and DNA bound Rad52 conditions, respectively. For clarity in discussion, we present the data from the perspective of the two halves of Rad52 and focus on the crosslinks between the two halves (Figs. 4A & B). Specifically, Lys-84, Lys-117, and Lys-134 in the N-terminal half make contacts with a defined region in the C-terminal half (residues 340-380; Fig. 4C). Lys-84 and Lys-117 are close to the outer ssDNA binding site whereas Lys-134 is the inner binding site residue (Fig. 4C). Closer examination of the interaction region in the C-terminal half reveals that it harbors the Rad51 binding site. Mutations in this region perturb Rad51 interactions and give rise to HR defects in yeast.[30,47] Given the abundance of conserved positively charged amino acid residues in this region, we term this the '*positive patch*' (Supplementary Fig. 13).

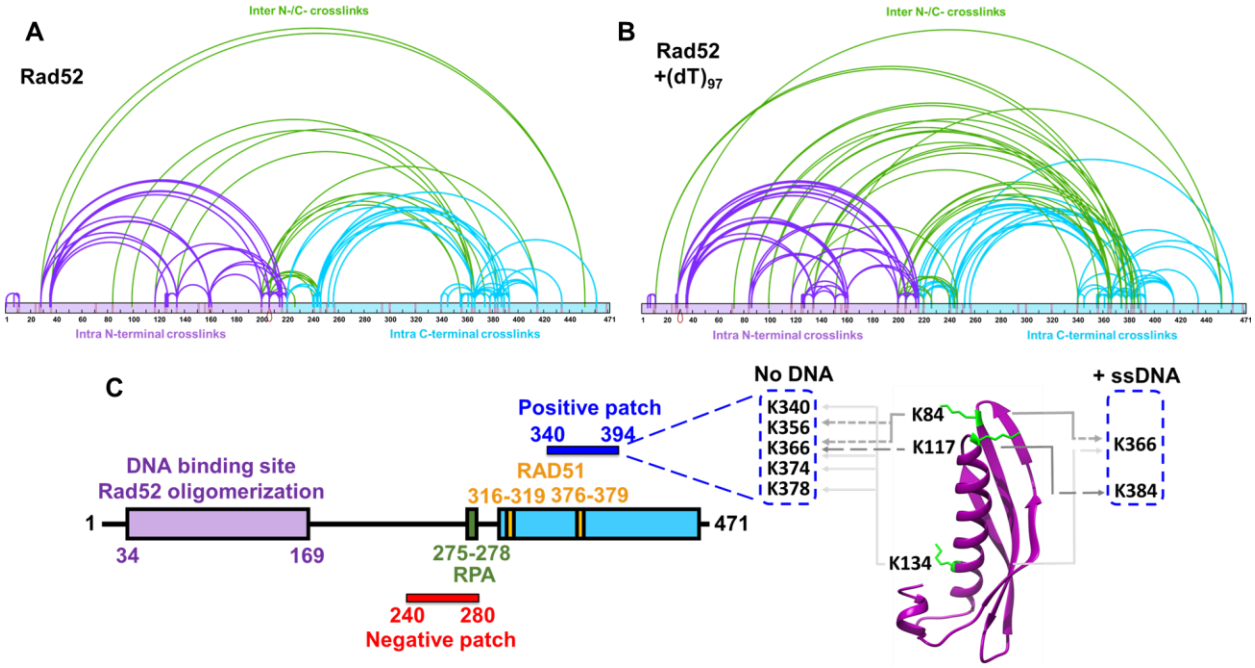

Figure 4. **Cross linking mass-spectrometry (XL-MS) reveals interactions between the N- and C-terminal halves of Rad52. A)** Rad52 or **B)** the Rad52-$(dT)_{97}$ complex was subject to crosslinking with BS3, and the resulting crosslinks were identified using MS. For clarity, data are mapped onto the N-terminal (purple) and C-terminal (yellow) halves of Rad52 as two distinct regions. Intra-N and intra-C half crosslinks are colored yellow and orange, respectively. Inter-crosslinks between the N- and C-terminal halves are colored green. **C)** Schematic representation of Rad52 shows positions of the RPA and Rad51 binding regions. The proposed positive and negative patches are denoted and the key crosslinks between the DNA binding sites, and the positive patch identified in the XL-MS analysis are highlighted.

Comparison of the crosslinks observed in the presence of ssDNA reveals both loss and gain of interactions (Fig 4). In particular, several of the crosslinks observed in the positive patch are lost (Fig 4B). These data suggest that ssDNA binding modulates interactions between the N- and C-terminal half of Rad52. In addition, substantial intra-C-terminal crosslinks are captured, suggesting that interactions within the disordered region might be important for function. We note that a conserved '*negative patch*' resides in the C-terminal half of Rad52 (residues 240-280) that harbors the site for RPA binding (Supplementary Fig. 13).[33] Significant crosslinks are observed between the positive and negative patches (Fig. 4). We propose that the network of interactions between the patches and the N-terminal half are likely important for function and may dictate the DNA binding and other functional properties of Rad52 (discussed below). Correspondingly, mutations in these patches result in loss of function phenotypes.[30,33,47]

The C-tail of Rad52 influences the dynamics of ssDNA wrapping

To decipher the contributions of the C-tail to Rad52 function, we first assessed the ssDNA binding activity of Rad52 mutants carrying deletions in either the C-terminal (Rad52$^{\Delta C}$; residues 1-217) or N-terminal (Rad52$^{\Delta N}$; residues 218-417) halves (Fig. 5A). In MP and AUC^{SV} analysis, majority of Rad52$^{\Delta C}$ behaves as a homodecamer and a smaller fraction (<5%) of higher order species of twice the mass (Fig. 5B and Supplementary Fig. 14A). In the cryo-EM analysis, 2D classes reveal that Rad52$^{\Delta C}$ also forms homodecameric rings in agreement with the N-terminal half harboring the oligomerization region (Supplementary Fig. 14B). ssDNA binding analysis reveal that Rad52$^{\Delta C}$ binds to ssDNA with high affinity (Fig. 5C & D), but monophasic binding is observed with a single site-size of 55±3 nt/decamer (Fig. 5C). Thus, the weaker second DNA binding phase with larger site-size is due to the influence of the C-tail (Fig. 2A). In addition, the Rad52$^{\Delta C}$ decamer binds to one molecule of ssDNA (Fig. 5B and Supplementary Fig. 14 B & C).

Although the C-tail appears to influence ssDNA binding in the context of full-length Rad52, the C-tail (Rad52$^{\Delta N}$ residues 218-471) does not bind to ssDNA (Fig. 5E). Interestingly, when Rad52-ssDNA interactions are measured in the presence of Rad52$^{\Delta N}$, a reduction in the weak second DNA binding phase is observed (Fig. 5F). Furthermore, when Rad52$^{\Delta C}$-ssDNA binding is measured in the presence of Rad52$^{\Delta N}$, a drastic reduction in the Trp quenching is observed (Fig. 5G). These data suggest that interactions between the N- and C-terminal halves of Rad52 influences binding or remodeling of ssDNA. A shorter version of the C-tail (Rad52$^{\Delta N*}$ residues

294-471) was shown to interact with ssDNA in band-shift analysis.[36] We observe weak ssDNA binding activity for Rad52$^{\Delta N*}$ (Fig. 5E). Challenging the ssDNA binding activity of Rad52$^{\Delta C}$ by addition of increasing concentrations of Rad52$^{\Delta N*}$ results in a robust loss of Trp fluorescence change (Fig. 5H). We reemphasize that Rad52$^{\Delta N}$ possesses both the positive and negative patches whereas the shorter Rad52$^{\Delta N*}$ protein carries only the positive patch (Fig. 5A). Since we detected crosslinks between these two patches in the C-terminus (Fig. 4), we propose that these two regions play opposing roles in regulating ssDNA binding. The positive patch may promote interactions with the phosphate backbone of ssDNA. The negative patch likely suppresses DNA binding/remodeling by sequestering away the positive patch.

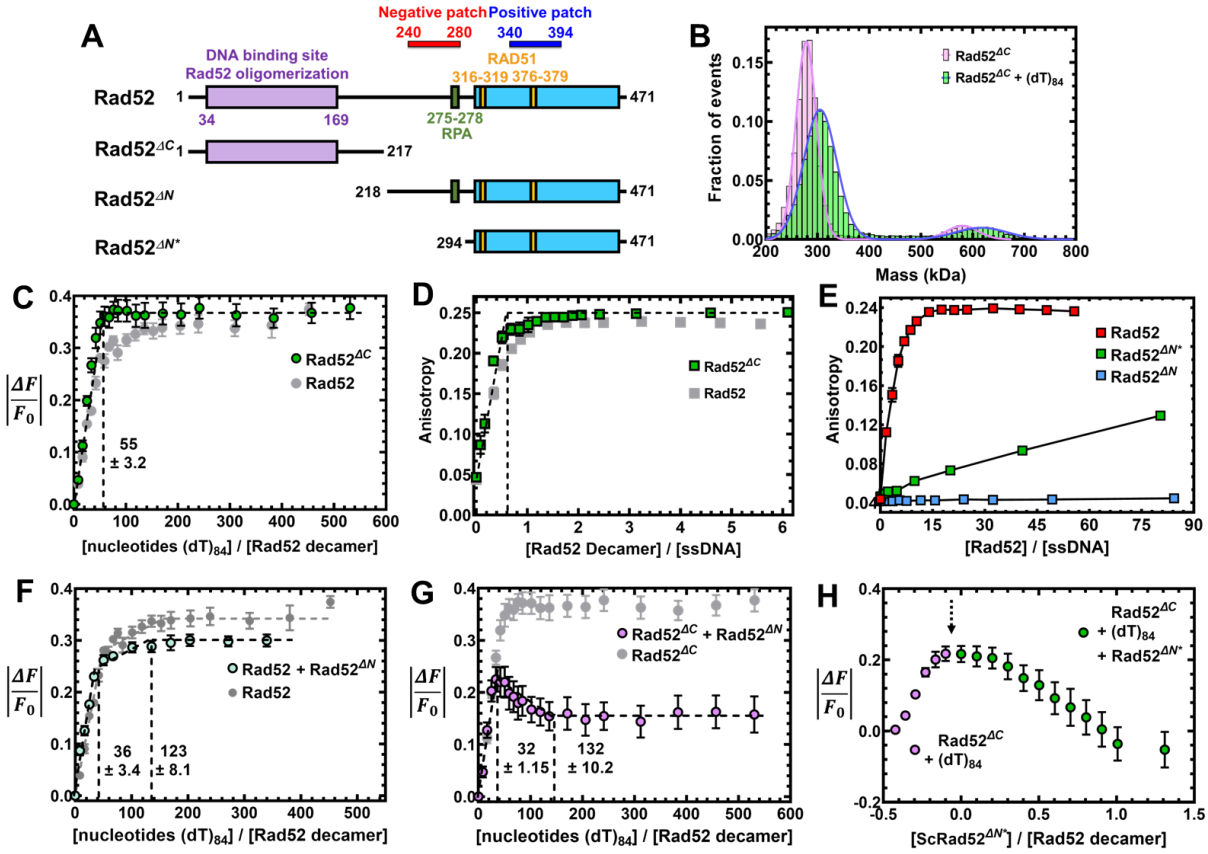

Figure 5. I**nteractions between the N- and C-terminal halves of Rad52 influence ssDNA binding interactions. A)** Schematic of the N- and C-terminal truncations of Rad52. **B)** Mass photometry analysis shows Rad52$^{\Delta C}$ as a predominant single species in solution with mass corresponding to a homodecamer (254.7±11.9 kDa). The complex remains a homodecamer when bound to ssDNA. **C)** Trp. quenching analysis of Rad52$^{\Delta C}$ binding to poly(dT) reveals high-affinity monophasic ssDNA binding with site-size of 55±3.2 nt/decamer. **D)** Fluorescence anisotropy analysis of Rad52$^{\Delta C}$ binding to a FAM-$(dT)_{35}$ oligonucleotide shows stoichiometric high affinity binding to ssDNA. **E)** Fluorescence anisotropy ssDNA binding analysis of N-terminal truncated versions of Rad52 show no ssDNA binding activity for Rad52$^{\Delta N}$, but weak binding for Rad52$^{\Delta N*}$. **F)** When Rad52$^{\Delta N}$ is premixed with Rad52, a reduction in the Trp quenching signal upon ssDNA $(dT)_{84}$ binding is observed. The signal corresponds to the loss of ssDNA to the low affinity binding site in Rad52. **G)** When Rad52$^{\Delta C}$ and Rad52$^{\Delta N}$ are premixed and binding to ssDNA $(dT)_{84}$ is assessed

through Trp. quenching, an initial increase in binding is observed as the high-affinity site is occupied. This was followed by a sharp loss in binding. **H)** When similar experiments are performed by sequential addition, titration of ssDNA $(dT)_{84}$ to Rad52$^{\Delta C}$ produces an increase in Trp quenching as expected (purple data points). After addition of ssDNA, increasing concentrations of Rad52$^{\Delta N*}$ was added, leading to loss in Trp quenching. This data shows defined regions in the C-terminal half of Rad52 modulate ssDNA binding interactions.

The C-tail regulates the dynamic movement/diffusion of Rad52 on ssDNA

Our data shows that the N-terminal half of Rad52 harbors the high-affinity ssDNA binding site and a significantly weaker DNA binding site in the C-terminal half (Fig. 5). Furthermore, a small subset of the C-tails interacts with the N-terminal region. Thus, we hypothesized that allostery and asymmetry might regulate the dynamics and diffusion of Rad52 on ssDNA. Functionally, such regulation could help position Rad52 at a defined position on the DNA (either at the ss-dsDNA junction or at the 3′ end). Using single-molecule total internal reflectance fluorescence (smTIRF) microscopy, we investigated the dynamics of Rad52 binding to DNA. Cy3 and Cy5 fluorophores were positioned on the DNA such that wrapping/unwrapping of DNA upon binding to Rad52 can be captured by following the changes in FRET. A ssDNA length of 45nt is sufficient to capture FRET (Supplementary Fig. 15). In the smFRET analysis, both Rad52 and Rad52$^{\Delta C}$ generate several FRET states that are higher than DNA alone (Figs. 6A-C and Supplementary Figs. 16 & 17). Rad52$^{\Delta C}$ samples the higher FRET states more frequently than Rad52 (Fig. 6B-E). These data again show that the C-terminal region can influence the DNA binding properties of Rad52.

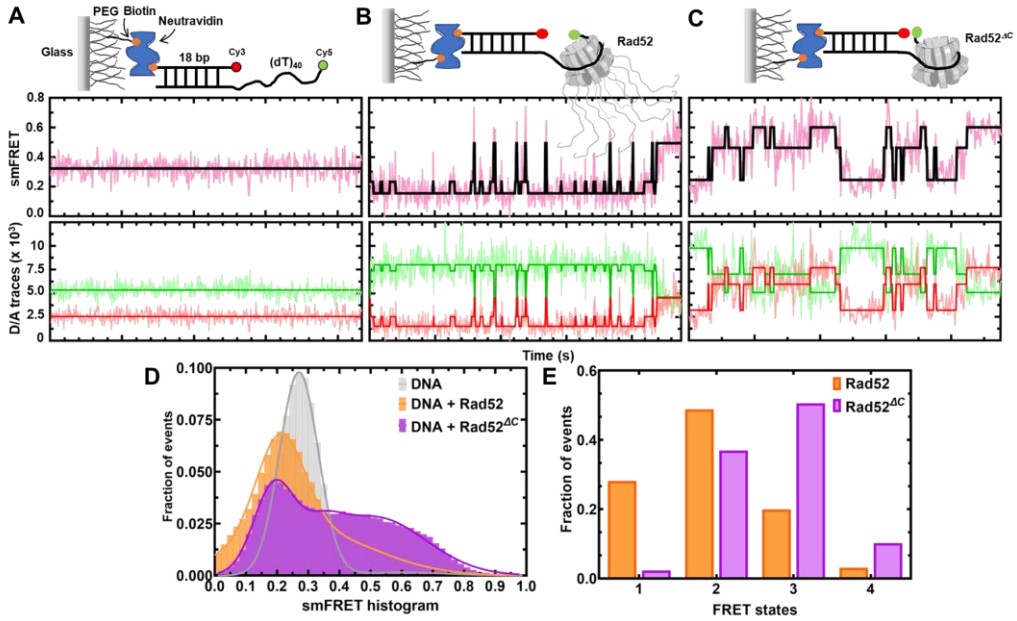

Figure 6. The C-terminus controls the intrinsic diffusion of Rad52 on ssDNA. Single-molecule FRET distributions of **A)** $(dT)_{40}$ overhang-ssDNA alone or $(dT)_{40}$ overhang bound to **B)** Rad52, or **C)** $Rad52^{\Delta C}$. **D)** & **E)** HMM analyzed FRET state distributions of smFRET traces show $Rad52^{\Delta C}$ accessing higher FRET states better than Rad52.

The C-tail induced asymmetry dictates Rad51 binding to a single Rad52 subunit.

In both the HDX-MS and cryo-EM analyses, only a select number of C-tails appears to asymmetrically interact with the N-terminus (Fig. 3G and Supplementary Fig. 12). Since the C-tails harbor Rad51 and RPA interaction sites, allosteric regulation of asymmetric binding of these proteins might be functionally important for Rad52 roles in HR. Thus, we investigated the interactions between Rad52 and Rad51 and the role of the C-terminus. Since each Rad52 subunit in the decamer possesses a Rad51 binding region, multiple Rad51 molecules can be expected to be coated around the ring. Furthermore, Rad51 forms multiple oligomeric complexes in solution as observed by AUC^{SV} (Fig. 7A) and MP (Supplementary Fig. 18). When Rad51 and Rad52 were mixed in equimolar amounts (1 Rad51 per Rad52 monomer) all the Rad51 molecules form a complex with the Rad52 decamer (Fig. 7A). Increasing the ratio of Rad51:Rad52 results in formation of complexes with higher molecular masses (Fig. 7A). Thus, we assumed that all subunits in the Rad52 ring were bound by Rad51. To better understand the structural organization of this complex we used single-particle Cryo-EM (Supplementary Fig. 19). Surprisingly, 2D classes show strong density for Rad51 bound alongside only one subunit in the Rad52 decamer (Supplementary Fig. 19A). Even when the concentration of Rad51 is doubled in the complex, selective binding to one part of the Rad52 ring is observed in the 2D classes (data not shown). Unfortunately, the dynamic nature of the complex and poor sampling of orientations hampered our ability to obtain high-resolution structures or reliable 3D volumes (Supplementary Fig. 19B). These studies imply that an intrinsic asymmetry within Rad52 exists and controls Rad51 interactions. This asymmetry and allostery was also observed in the interactions between the C-tails and the N-terminal half of Rad52 (Fig. 3). Deletion of the C-terminal tail ($Rad52^{\Delta C}$) reduced complex formation with Rad51 and more polydisperse complexes were observed (Supplemental Fig. 20). Thus, it is likely that the C-tail allosterically contributes to modulation of Rad52-Rad51 binding asymmetry. In addition, since Rad51 binds to $Rad52^{\Delta C}$, a binding site for Rad51 exists within the N-terminal half of Rad52.

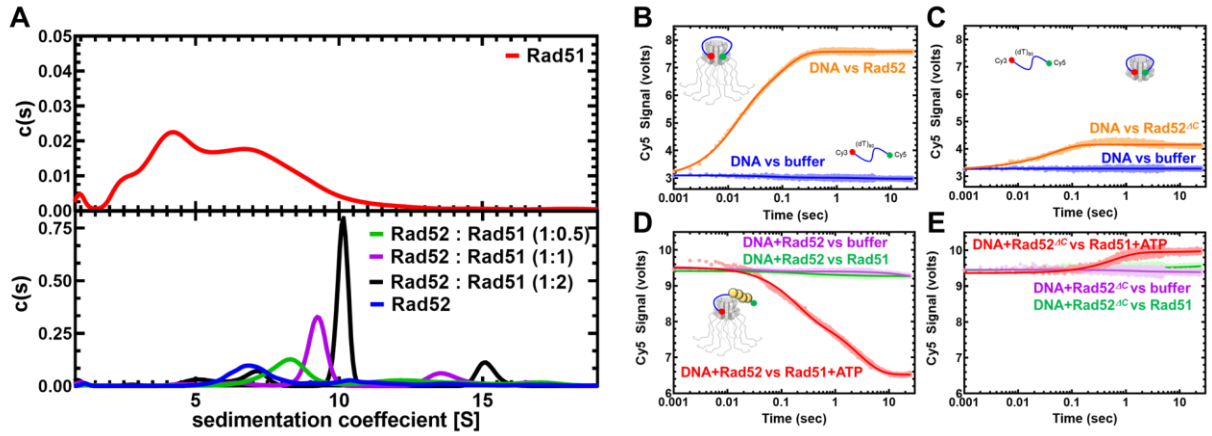

Figure 7. The C-tail of Rad52 regulates allosteric interactions with Rad51. A) AUC^{SV} analysis (top panel) shows polydispersity of Rad51 with multiple oligomeric states. When increasing amounts of Rad51 (1, 10, or 10μM) are mixed with a fixed concentration of Rad52 (10μM monomer), formation of Rad52-Rad51 complexes is observed. The size of the complexes increases as a function of Rad51 concentration in the solution. **B)** Stopped flow FRET experiments were performed with a $(dT)_{97}$ ssDNA labeled at the ends with Cy3 (3′; donor) and Cy5 (5′; acceptor). In the absence of protein, no changes in FRET are observed (blue) and a robust increase is captured when Rad52 is introduced (orange). Similar experiments done with **C)** Rad52$^{\Delta C}$ show wrapping of ssDNA. **D)** FRET experiments were performed using prewrapped Rad52-ssDNA complexes and change in FRET was measured upon addition of Rad52 in the absence (green) or presence (red) of ATP. A loss in FRET is observed when Rad51 filaments are formed on the ssDNA in the presence of ATP. **E)** Similar experiments performed with Rad52$^{\Delta C}$ do not show a decrease in FRET suggesting an impediment to Rad51 filament formation.

Formation of proper Rad51 filaments requires the C-tail of Rad52

To investigate the role of Rad52 in promoting Rad51 binding to ssDNA and formation of a filament, we utilized a FRET assay using end-labeled ssDNA oligonucleotides. Cy3 (donor) and Cy5 (acceptor) were positioned at the 3′ and 5′ end of a $(dT)_{97}$ ssDNA oligonucleotide and changes in Cy5 fluorescence were measured by exciting Cy3. Upon binding to Rad52 or Rad52$^{\Delta C}$, the ssDNA is wrapped around the decameric ring, and the fluorophores are brought in proximity resulting in high FRET-induced Cy5 fluorescence (Figs. 7A & B). The experiments were conducted in a stopped flow instrument and the kinetics of Cy5 fluorescence change was monitored. Next, preformed Rad52-DNA or Rad52$^{\Delta C}$-DNA complexes were challenged with Rad51 in the absence or presence of ATP. ATP-binding promotes Rad51 binding and filament formation[48], and thus, in the presence of ATP a rapid loss in the FRET signal is observed in experiments with Rad52 (Fig. 7D). In contrast, no reduction in FRET was observed for the Rad52$^{\Delta C}$-DNA complex suggesting that Rad51 does not immediately form a filament when the C-terminal half of Rad52 is absent (Fig. 7E). Interestingly, a minor increase in the FRET signal is observed which reflects Rad51 binding directly to ssDNA as free DNA would be available when

Rad52$^{\Delta C}$ is wrapped by a $(dT)_{97}$ substrate (Supplementary Fig. 15). Please note that these changes are only captured in shorter time regimes in the stopped flow experiments. In steady state FRET measurements, Rad51 eventually outcompetes both Rad52 and Rad52$^{\Delta C}$ leading to similar signal changes (Supplemental Fig. 21 B & C). Thus, the C-terminus of Rad52 regulates formation of Rad51 filaments on ssDNA.

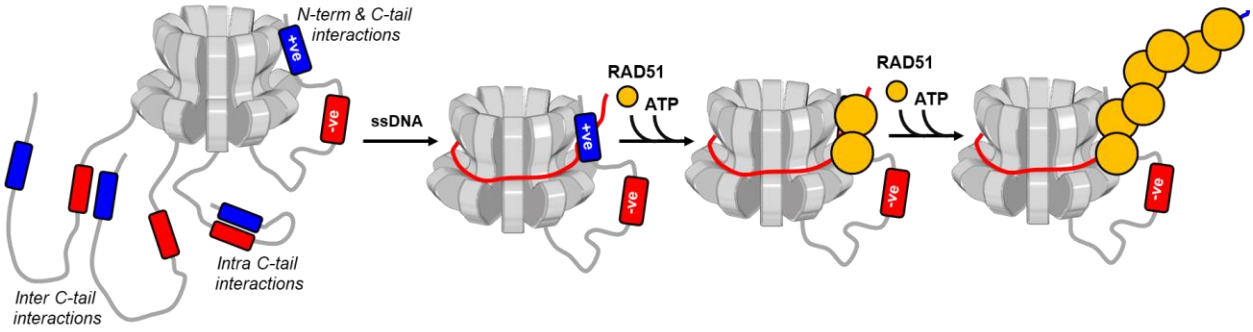

Figure 7. Model describing the mechanism of action of Rad52 and regulation by the C-tail. The homodecameric ring structure of the N-terminal half of *S. cerevisiae* was depicted and three of the ten disordered C-terminal tails were shown (for clarity). The negative and positive patches were shown and the asymmetric interaction between one tail and the N-terminal half was depicted. We propose that such interactions in remaining tails were allosterically suppressed through either intra or inter C-tail interactions between the negative and positive patches. The path of ssDNA binding is modulated through interactions between the DNA backbone and the positive patch bound to the N-terminal half. This unique asymmetric region of interaction between the two halves of Rad52 serves as the point of Rad51 binding and nucleation on to ssDNA. In the presence of ATP, this allosterically controlled process promotes *single-position nucleation and growth* of presynaptic Rad51 filaments in HR.

Discussion

A barebones view of events during formation of the Rad51 filament during HR pre-synapsis encompasses a resected 3′ ssDNA overhang coated by RPA, Rad51, and Rad52. Previous models suggested that the mediator functions of Rad52 promote removal of the high-affinity DNA binding RPA (K_D <10^{-10} M) to enable binding/nucleation of the lower affinity Rad51 (K_D ~10^{-6} M)[49]. Physical interactions between heptameric Rad52 and Rad51 and RPA are required for this exchange[30,34,50]. Recent single-molecule experiments show that RPA-Rad52 function as a complex on the DNA to promote Rad51 binding, with additional roles in downstream second-strand capture[51]. In terms of the structure-function assessments, the N-terminal half of each Rad52 subunit is thought to promote the oligomerization and DNA binding activities[23,24,37,52]. Protein-interaction domains have been mapped to the C-terminal half[22,30,53-55]. How the various activities of Rad52 are coordinated to enable the mediator functions in HR are poorly resolved.

Using single-particle cryo-EM analysis, we illustrate that *S. cerevisiae* Rad52 functions as a homodecamer. As shown for human Rad52, the N-terminal half is ordered in the homodecameric ring architecture, and the C-terminal half is disordered. Remarkably, an intrinsic asymmetry in Rad52 is imparted by the C-terminal region from one (or a select few) subunit that interacts with the ordered ring. This asymmetry in turn regulates a two-state ssDNA activity driven through high- and low-affinity ssDNA binding interactions. When the C-tail is removed, the low-affinity binding is lost. We propose the presence of two charged regions (termed as positive and negative patches) in the C-tail that contribute to the asymmetry within Rad52. The positive patch interacts weakly with ssDNA, and interactions between the positive and negative patches inhibit this activity. In the subunits where interactions between the N- and C-terminal halves are observed, the positive charge is accessible to ssDNA interactions. We speculate that such asymmetric interactions could guide the path of ssDNA around the Rad52 ring and likely setups either polarity or define the position of Rad51 or RPA binding (Fig. 8).

In support of this model, the asymmetry identified in the Rad52 structure also extends to interactions with Rad51. In cryo-EM 2D class averages, Rad51is bound to only one region in the Rad52 ring (Supplementary Fig. 19). This observation persists even when a vast excess of Rad51 is present in the reaction. These data suggest that the asymmetry in ssDNA and Rad51 binding within Rad52 might serve as a mechanism for 'single-position nucleation' of the Rad51 nucleoprotein filament (Fig. 8). This phenomenon might be essential for accurate DNA repair in HR. Identification of perfect homology within the undamaged strand (sister allele) is of paramount importance[56]. For Rad51 (and the prokaryotic homolog RecA) a minimum of 8 nt homology is required to promote strand invasion[57-60]. Furthermore, a 'search entity' has been proposed where Rad51 is in complex with additional proteins (including Rad52 and RPA) to catalyze homology search and pairing[56]. Thus, if Rad51 binds to multiple subunits on Rad52, formation of a uniform search entity that engages and handles ssDNA at a single position might not be possible. We envision a minimal search entity to contain a Rad52 decamer bound to Rad51 at a single defined position. This binding position is dictated by one (or a select few) of the C-tails that interacts with both the ordered N-terminal half and ssDNA. The mechanisms of negative cooperativity and allostery enacted to suppress such binding events in the other C-tails in the Rad52 ring needs to be deciphered. The positive patch we define also harbors the Rad51 binding motif. Thus, the C-terminal ssDNA and Rad51 binding sites are likely coupled.

Another layer of complexity is the position of RPA within the RPA-Rad52-Rad5 complex. Does the minimal search entity comprise RPA-Rad52-Rad51? Does the RPA-Rad52 complex form first and then recruit Rad51, or is it the inverse? Can such complexes be formed in the absence of ssDNA? Many such questions need to be answered. In the absence of ssDNA we can reliably capture the RPA-Rad52-Rad51 complex in analytical ultracentrifugation analysis (Supplementary Fig. 21). Using single-molecule tools, we previously showed that Rad52 can selectively remodel DNA-binding domain D of RPA of an RPA-ssDNA complex[61]. In the absence of ssDNA, the Rtt105 chaperone inhibits interactions between Rad52 and RPA by configurationally stapling the flexible architecture of RPA[62]. Thus, many other regulatory mechanisms need to be accounted for to comprehensively understand the nature of the 'search entity' and its regulation.

Acknowledgements

The authors thank members of our respective research laboratories for critical reading of the manuscript. This work was supported by grants from the National Institutes of Health (R01 GM130746 and R01 GM133967) to E.A. Funding for Proteomics, Metabolomics and Mass Spectrometry Facility at MSU was made possible in part by the MJ Murdock Charitable Trust and NIGMS of the National Institutes of Health under Award Number P20 GM103474. The analytical ultracentrifugation experiments were supported by an instrumentation grant from the Office of the Director, National Institutes of Health (S10 OD030343 to E.A.). M.J.R, and K.B. gratefully acknowledge support from the Washington University Center for Cellular Imaging (WUCCI) which is funded by Washington University School of Medicine, The Children's Discovery Institute of Washington University and St. Louis Children's Hospital (CDI-CORE-2015-505 and CDI-CORE-2019-813), the Foundation for Barnes-Jewish Hospital (3770) and the Alvin J. Siteman Cancer Center at Washington University School of Medicine and Barnes-Jewish Hospital under NCI Cancer Center Support Grant P30CA091842. J.A.J.F gratefully acknowledges the Chan Zuckerberg Initiative for their support as a CZI Imaging Scientist under award 2020-225726.

Author Contributions

J.D., M.J.R., K.B. and J.A.J.F. collected single-particle cryo-EM data and solved the structure. R.C. performed fluorescence and single-molecule experiments. J.M. and B.B. performed and analyzed the HDX-MS and XL-MS experiments. S.K., N.P., and N.E. assisted with cloning,

protein purification, and experiments. E.A. conceived the project and wrote the manuscript with assistance and contributions from all authors.

Data availability

Raw data for all the experiments are provided in the *Source Data* file and available with the manuscript. Clones for protein expression are available upon request. Structural data have been deposited in the PDB.

Competing interests

The authors declare no competing interests.

Materials and Methods

Reagents and Chemicals

Fluorescently labeled and non-labeled oligonucleotides were ordered from Integrated DNA technologies Inc. Poly(dT)was purchased from Midland Certified Reagent Company. Chemicals were purchased from Millipore-Sigma, Research Products International, Gold Biotechnology, and Fisher Scientific. Resins for protein purification were from Cytiva Life Sciences, Bio-Rad laboratories, and Gold Biotechnology.

Plasmids for protein overproduction

Plasmids carrying the coding sequence for yeast Rad52 with a cleavable C-terminal chitin binding domain (CBD) was a kind gift from Dr. Eric Greene (Columbia University). *Rad52$^{\Delta C}$* was generated by introducing a stop codon at the nucleotide position corresponding to amino acid position 218. *Rad52$^{\Delta N}$* and *Rad52$^{\Delta N*}$* were generated by PCR amplifying the respective fragments and subcloning into xxx. Plasmids for overproduction of RPA and Rad51

Purification of Rad52 and Rad52 mutants

The respective pTXB1 plasmids were generated by cloning Rad52 PCR fragments (Rad52$^{\Delta C}$, Rad52$^{\Delta N}$ and Rad52$^{\Delta N*}$) using *NdeI* and *XhoI* restriction sites. Rad52 plasmids were transformed into RossettaRosetta-2 PlysS cells, plated on LB agar plates (with 100 μg/mL ampicillin), and incubated overnight at 37 °C. A single colony was inoculated in a 50 mL LB starter culture supplemented with ampicillin and incubated overnight at 250 rpm at 37 ^{o}C. 10 mL of overnight culture was inoculated into aa 2.8 L baffle flask with 1.5 L LB media supplemented with ampicillin and grown at 250 rpm at 37 ^{o}C until the growth reached an OD_{600} of 0.6. The culture was induced by thethe addition of 1 M IPTG (0.5 mM). Following induction, the culture was incubated overnight at 150 rpm, 18 ^{o}C. All the steps from here on were performed at 4 ^{o}C or on ice. Cells were pelleted by centrifugation at 5000 rpm for 30 minutes and resuspended in 200 mL cell lysis buffer (50 mM Tris-HCl, pH 8.0; 600 mM NaCl; 1 mM EDTA, pH 8.0; 2X PIC). Cells were lysed by incubation for 30minutes with lysozyme at 4 °C, followed by 2 cycles of sonication with 50 % amplitude; 2 seconds pulses for 60 seconds, followed by (?) a pause for additional 1 minute. Cell lysate was clarified by centrifugation at 17 000rpm for 1 hour. The clarified supernatant was then batch-bound for 3 hours on to 20 mL chitin resin (NEB, Ipswich, MA) equilibrated with 200 mL of cell lysis buffer. Flow-through was collected and the resin was sequentially washed with 100 mL each of cell lysis buffer, cell lysis buffer + 1.5 M NaCl and finally with the cell lysis buffer. Bound Rad52 protein was batch eluted with CBD elution buffer (cell lysis buffer + 50 mM DTT). Chitin column eluates were analyzed by 10 % SDS-PAGE and eluates containing Rad52 were pooled, diluted with R_0 (50 mM Tris-HCl pH 7.5, 1 mM EDTA pH 8.0, 2 mM βME, 10 % glycerol, 2X PIC) to a final conductivity of R_{200} and applied on 20 mL heparin column (Cytiva, Marlborough, MA, USA). Bound Rad52 was fractioned using a linear gradient of R_{200}-R_{1000}. The eluted fractions were analyzed by 10 % SDS-PAGE, and fractions containing Rad52 were pooled and loaded on 20 mL Q-column. The eluted fractions were analyzed by 10 % SDS-PAGE, and fractions containing Rad52 were pooled, concentrated with a 30 kDa cut-off spin concentrator to a volume less than 5 mL and applied on to HiLoad 16/600 200 Superdex-200 pg size exclusion column. S200 fractions were further analyzed by 10 % SDS-PAGE and those containing Rad52 were pooled, concentrated with a 30 kDa cut-off spin concentrator, and stored at -80 °C as small aliquots after flash freezing with liquid nitrogen. Before

flash freezing, concentration of Rad52 was determined spectroscopically using OD_{280}, with correction using OD_{350} and molar extinction coefficient (ε_M) 25900 $M^{-1}cm^{-1}$. $Rad52^{\Delta N}$, and $Rad52^{\Delta N*}$ lack Tryptophan residues so their concentration was estimated using the predicted molar extinction coefficient for the peptide bond measured at 214 nm. In addition, the concentration of Rad52, $Rad52^{\Delta C}$, $Rad52^{\Delta N}$, and $Rad52^{\Delta N*}$were also verified using Bradford assay before performing Tryptophan quenching experiments. Rad51 was purified as described previously (Conway et al 2004). Protein concentration for Rad51 is determined spectroscopically using OD_{280} molar extinction coefficient (ε_M) 11920 $M^{-1}cm^{-1}$

Determination of stoichiometry and molecular weight using Mass Photometry

Mass photometry measurements were carried out on a TwoMP instrument (Refeyn Inc.). Glass coverslips (No. 1.5H thickness, 24x50mm, VWR) were cleaned by sonication, first in isopropanol, and then in deionized water for 15min. Cleaned coverslips were dried under a stream of nitrogen. For some measurements (e.g., DNA-bound complexes) coverslips were coated with a 0.1% w/v poly-lysine solution. For each measurement, a clean coverslip with a 6-well silicone gasket was placed onto the water-immersion objective and samples were added onto each well as described below. Molecular weight standards were resuspended in the respective matching buffers and used to calibrate and convert the image contrast due to scattered light into MW units. Rad52 from Q-column fractions 1, and 2 were dissolved to a final concentration of 130nM decamers (or 1.3µM monomers) in 1X buffer. After focus was obtained and the image stabilized, 1uL of the 130nM protein solution was injected into 15µL of 1X buffer taken in a silicon gasket well resulting in a 8.1nM solution of decamers. The solution was pipetted in/out twice to mix followed by a 60s video recording. 8-10nM concentration of Rad52 decamers was optimum to give molecular weight (MW) units. Standards included beta-Amylase (3 species of 56, 112, 224 kDa) and Thyroglobulin (one species of 667 kDa). The denoted concentration of protein or complexes in the appropriate buffer were used for the measurements. First, 15 µl of the buffer was first added to the well and focus was obtained, and the image stabilized. Next, 1 µl of stock protein in the same buffer was mixed into the well and image acquisition was immediately initiated. Images were collected for 60s total. For Rad52, 1 µl of 130 nM decamer (1.3 µM monomers) was mixed with 15 µl of buffer in the well to obtain 8.1 nM decamers during the measurements. 8-10 nM of Rad52 decamers produced statistically significant number of particles (~5,000) over a 60 s recording. For data analysis, single particle landings (events) were converted to mass units using the standard calibration, extracted from videos, and non-linear least squares fitted with Gaussian mixture model (Eq. 1) to discern underlying populations corresponding to free monomers (60-70gm/Mole; < 5%), and twice the mw of decamers 1010-1025kDa, likely representing two fused rings or other multimeric species. Upon addition of $(dT)_{84}$ (25.4kDa), the molecular weight of the 3 populations didn't appear to shift noticebly. This is likely since the limit of sensitivity of the instrument is ~ 50kDa and any increments in molecular weight lower thanthan that are likely hard to distinguish from measurement noise. namely,

$$f(x) = \mathrm{a}_1 * exp^{-\left(\frac{x-b_1}{c_1}\right)^2} + \mathrm{a}_2 * exp^{-\left(\frac{x-b_2}{c_2}\right)^2} + \cdots \mathrm{a}_n * exp^{-\left(\frac{x-b_n}{c_n}\right)^2} \quad \ldots. (1)$$

Where a_n , b_n, and c_n are the amplitude, mean, and the standard deviation of the n^{th} Gaussian component. For Rad52 and $Rad52^{\Delta C}$, the n equaled 3, but Rad51 showed significant heterogeneity and the Rad51 nano-filament mass size ranged from a dimer to a pentadecamer ($n = 15$).

Analytical Ultracentrifuge (AUC) Analysis

Analytical ultracentrifugation sedimentation velocity experiments were performed with an Optima Analytical Ultracentrifuge (Beckman-Coulter Inc.) using a An-50 Ti rotor. Samples were spun at of 40,000 rpm at 20 °C. Samples were prepared by thoroughly dialyzing against 30 mM HEPES, pH 7.8, 100 mM KCl, 10% glycerol, and 1 mM TCEP. Sample (380 µL) and buffer (400 µL) were filled in each sector of 2-sector charcoal quartz cells. Absorbance was monitored at 280 nm for samples using absorbance optics and scans were obtained at 3 min intervals. The density and viscosity of the buffer at 20°C was calculated using SEDNTERP. The continuous distribution sedimentation coefficient (c(s)) model was used to fit the AUC data using SEDFIT.[63]

Cryo-EM Data collection

3 µL of 0.31mg/mL Rad52 or 0.44mg/mL Rad51-Rad52 were applied to Quantifoil R 2/2 300 copper mesh grids, then plunge-frozen into liquid ethane using a Vitrobot Mark IV (Thermo Fisher Scientific, Brno, Czech Republic) set to 4°C and 100% humidity. Prior to vitrification, the grids were plasma cleaned in an H_2O_2 plasma for 1 minute using a Solarus 950 (Gatan, Warrendale, PA). The sample was allowed to incubate for 20s on the grids prior to blotting. Single-particle cryo-EM data was acquired on a 200 kV Glacios cryo-TEM equipped with a Falcon IV direct electron detector (Thermo Fisher Scientific, Eindhoven, Netherlands). The nominal magnification was 150,000x, resulting in a pixel size of 0.94Å. The total electron dose was 50.7 $e^{-}/Å^2$ per movie with 48 frames, and the defocus value varied between -0.8 and -2.4µm.

Cryo-EM Image processing

Single-particle cryo-EM data was processed using cryoSPARC v3.2.0.[64] For the Rad52 dataset, 2,447 raw movies were motion corrected using patch motion correction, then the CTF estimation of the subsequent micrographs was performed using patch CTF estimation. Initial particle picking was accomplished using blob picker, the results of which were subjected to 2D classification. The best templates were chosen for a subsequent template picker job. After inspection of the template picks, 701,962 particles were extracted using a box size of 300 pixels and subjected to three rounds of 2D classification, resulting in 180,545 particles. Three initial models were generated using an *ab-initio* reconstruction job, which were then refined by a heterogeneous refinement job with C1 symmetry. After visualizing the volumes in UCSF ChimeraX[65] the best class (consisting of 46,845 particles) was chosen for further processing. The class was subjected to non-uniform refinement with C10 symmetry, then the particle stack was symmetry expanded and underwent local refinement. The resulting cryo-EM density map had an estimated gold standard Fourier shell correlation (FSC) resolution of 3.48 Å at a threshold of 0.143.

Model building:

The Atomic model for yeast rad52 was built *de novo* using Model Angelo tool (https://doi.org/10.48550/arXiv.2210.00006). Model Angelo generated model was curated manually in chimera and coot v0.9.3. The manually curated atomic model was real space refined followed by manual curation in coot. The final model was validated by Ramachandran plot in phenix.

Solution conditions for measurements

To readily match results across various assays, every effort was made to keep the solution conditions identical in various measurements. All measurements performed on fluorimeter, mass photometer, stopped-flow, and the single-molecule microscope in 1X reaction buffer (50mM Tris acetate pH 7.5, 50mM KCl, 5mM $MgCl_2$, 10% glycerol, 1mM DTT, and 0.2mg/mL BSA). For instance, BSA was omitted from all Trp quenching, and mass photometer experiments. DTT was omitted from single-molecule imaging. And 2.5mM ATP was included in Rad52-Rad51 DNA handoff experiments whether done at equilibrium in fluorimeter or on the stopped-flow instrument to estimate the pre-steady state kinetics. Where possible the temperature was maintained constant at 23°C.

Measurement of ssDNA binding to Rad52 using fluorescence anisotropy

5′-FAM labeled $(dT)_{35}$ or $(dT)_{70}$ ssDNA was diluted to 30 nM in 50 mM Tris-Acetate pH 7.5, 50 mM KCl, 5 mM $MgCl_2$, 10% v/v glycerol, 1 mM DTT, and 0.2 mg/mL Bovine Serum Albumin Fraction V (BSA) and taken in a 10 mm pathlength cuvette (Starna cells). The temperature was maintained at 23°C as the fluorescein labelled-ssDNA molecules were excited with vertically polarized 488 nm light and any emission was collected using a 520 nm bandpass filter in parallel and perpendicular orientation using PC1 spectrofluorometer (ISS). The samples were taken in triplicate and five consecutive measurements were averaged for each data point as G-factor corrected anisotropy values were measured after each addition of Rad52 (full-length or Rad52$^{\Delta C}$). The addition of protein continued until the anisotropy plateaued indicating an end to the titration. The raw anisotropy values were corrected for the reduction in quantum yield of the fluorescein moiety upon Rad52 addition, brought about the proximity based quenching effects of the bound protein molecule as follows,

$$A_c = \frac{\left[\left(\frac{A - A_f}{A_b - A}\right) \times \left(\frac{Q_f}{Q_b}\right) \times (A_b)\right] + A_f}{1 + \left[\left(\frac{A - A_f}{A_b - A}\right) \times \left(\frac{Q_f}{Q_b}\right)\right]} \quad \ldots. (2)$$

Where, 1) F_b, and F_f are the bound, and free concentrations of the FAM-labeled fluorescent ssDNA in nM, 2) Q_b, and Q_f are the fluorescence quantum yields of the bound and free form of the FAM-labeled fluorescent ssDNA (arbitrary units), 3) A_b, and A_f are the anisotropy values of the bound, and free forms of the FAM-labeled fluorescent ssDNA, 4) A, is the measured anisotropy, and 5) A_c is the corrected anisotropy value. Care was taken to limit the maximal dilution to <5% of initial volume and the protein, and ssDNA concentration was corrected for this effect. Due to extremely tight binding between Rad52 (full length, and Rad52$^{\Delta C}$), and $(dT)_{35}$, no attempt was made to fit a binding curve to the data points. This kind of stoichiometric binding has been observed earlier for other single stranded DNA binding proteins, most notably RPA and SSB.

Tryptophan quenching assays

Titrations monitoring the tryptophan fluorescence output of Rad52 (full length or Rad52$^{\Delta C}$) were performed with PC1 spectrofluorometer (ISS). The Tryptophan residues in the protein samples were selectively excited with 296 nm excitation light and the emitted fluorescence (320 – 360 nm) was collected as a scan in triplicate using a 10 mm path length cuvette; The peak being located at 345 nm. The temperature of the sample was maintained at 23°C. ssDNA (poly(dT) or $(dT)_{84}$) was added to a 1.2 mL, 50 nM (full length or Rad52$^{\Delta C}$ decamer concentration) protein taken in 50 mM Tris-Acetate pH 7.5, 50 mM KCl, 5 mM $MgCl_2$, 10% v/v glycerol, and 1 mM DTT with constant stirring. After a 2 min incubation, the fluorescence emission scan was acquired.

To minimize photobleaching the excitation shutter waswas only open during the data acquisition. The fluorescence values were corrected for the effects of dilution, photobleaching, and inner filter effects.

$$F_{i,corr} = F_{i,raw} \times \left(\frac{V_{i,raw}}{V_0}\right) \times \left(\frac{1}{C}\right) \times \left(\frac{f_0}{f_i}\right) \quad \ldots. (3)$$

Where, $F_{i,raw}$, and $F_{i,corr}$ are measured, and corrected Rad52 fluorescence values after each (i^{th}) addition of nucleic acid stock. V_0 is the initial volume of the solution before titration, V_i is the volume after after addition of the ith aliquot. f_0 , and f_i are the initial fluorescence and fluorescence of Rad52 due to photobleaching alone under identical solution conditions. C or the correction factor for the inner filter effect was assumed to be 1 because of following reasons: 1) The optical density (OD_{280}) of Rad52 at 50nM decamer concentration (or 0.5 µM monomer concentration) is only 0.013 which is at least 7 fold lower than the O.D. = 0.1 cutoff where inner filter effects become significant, 2) In addition, the normalized fluorescence spectra of Rad52 at 10, 25, 50, and 70nM decamer concentration appear comparable (data not shown), 3) the maximum concentration of ssDNA in the cuvette, at the end of titration, rarely exceeded 250 nM. The corrected data was plotted as the absolute change in fluorescence normalized to the initial fluorescence ($\left|\frac{\triangle F}{F_0}\right|$) on Y-axis, with [nucleotides] / [Protein] ratio on the X-axis. The biphasic curve resultant from the TRP quenching of Rad52 with poly(dT) or $(dT)_{84}$ could be fitted with a model for two independent, sequential DNA binding sites as follows:

$$TQ = \frac{TQ_1 K_{D1} D_f + TQ_2 K_{D1} K_{D2} D_f^2}{1 + K_{D1} D_f + K_{D1} K_{D2} D_f^2} \quad \ldots. (4)$$

$$D = D_f + D_b = D_f + \frac{K_{D1} D_f + 2K_{D1} K_{D2} D_f^2}{1 + K_{D1} D_f + K_{D1} K_{D2} D_f^2} [Rad52] \quad \ldots. (5)$$

Where, TQ is the observed Tryptophan quenching, which is sum of two components TQ_1, and TQ_2 due to the strong and the weak binding components. K_{D1}, and K_{D2} are macroscopic dissociation constants for the first and the second phase, respectively. D is the total DNA concentration which is sum of free and bound components D_f, and D_b. Note that D_b is a function of total protein concentration or [Rad52]. [$Rad52$] is assumed to bebe constant at 50 nM (decamer) during fitting as there is less than 5% dilution by the end of titration. K_{D1}, and K_{D2} are determined from the non-linear least squares fitting of equations 2, and 3.

Hydrogen-Deuterium Exchange mass spectrometry (HDX-MS) analysis

Stock solutions of Rad52 (15.3 mg/mL) were mixed in the presence or absence of $(dT)_{97}$ ssDNA in a 1:1.2 ratio. Reactions were diluted 1:10 into deuterated reaction buffer (30 mM HEPES, 200 mM KCl, pH 7.8). Control samples were diluted into a non-deuterated reaction buffer. At each time point (0, 0.008, 0.05, 0.5, 3, 30 h), 10 µL of the reaction was removed and quenched by adding 60 µL of 0.75% formic acid (FA, Sigma) and 0.25 mg/mL porcine pepsin (Sigma) at

pH 2.5 on ice. Each sample was digested for 2 min with vortexing every 30 s and flash-frozen in liquid nitrogen. Samples were stored in liquid nitrogen until the LC-MS analysis. LC-MS analysis of Rad52 was completed as described [66] Briefly, the LC-MS analysis of Rad52 was completed on a 1290 UPLC series chromatography stack (Agilent Technologies) coupled with a 6538 UHD Accurate-Mass QTOF LC/MS mass spectrometer (Agilent Technologies). Peptides were separated on a reverse phase column (Phenomenex Onyx Monolithic C18 column, 100x2mm) at 1°C using a flow rate of 500 µL/min under the following conditions: 1.0 min, 5% B; 1.0 to 9.0 min, 5 to 45% B; 9.0 to 11.8 min, 45 to 95% B; 11.8 to 12.0 min, 5% B; solvent A = 0.1% FA (Sigma) in water (Thermo Fisher) and solvent B = 0.1% FA in acetonitrile (Thermo Fisher). Data were acquired at 2 Hz s^{-1} over the scan range 50 to 1700 m/z in the positive mode. Electrospray settings were as follows: the nebulizer set to 3.7 bar, drying gas at 8.0 L/min, drying temperature at 350°C, and capillary voltage at 3.5 kV. Peptides were identified as previously described [67] using Mass Hunter Qualitative Analysis, version 6.0 (Agilent Technologies), Peptide Analysis Worksheet (ProteoMetrics LLC), and PeptideShaker, version 1.16.42, paired with SearchGUI, version 3.3.16 (CompOmics). Deuterium uptake was deter- mined and manually confirmed using HDExaminer, version 2.5.1 (Sierra Analytics). Heat maps were created using MSTools [68].

Crosslinking Mass Spectrometry (XL-MS) analysis

Stock solutions of Rad52 (15.3 mg/mL) and ssDNA $(dT)_{97}$ (conc.) were diluted to 1.8 mg/mL and 2.2 mg/mL, respectively in buffer (30mM HEPES, 200mM KCl, pH 7.8 and incubated together for 30min. The diluted proteins were reacted with primary amine reactive 5 mM bis(sulphosuccinimidyl)suberate (BS3) and 20 µL of the sample was taken at various time points (0, 15, and 30 minutes) and immediately quenched with 2 µL of 1 M ammonium acetate. Quenched samples were diluted with 1.5X Laemmli gel loading buffer to a final volume of 40 µL, vortexed, and heated to 100°C for 5 min and resolved on 4-20% (w/v) gradient SDS-PAGE gels (Bio-Rad) with Tris-glycine buffer. Gels were stained with Gelcode blue safe protein stain (Thermo Scientific). Gel bands were excised for protein identification and analysis. Excised bands were destained with a 50 mM ammonium bicarbonate and 50% acetonitrile mixture and reduced with a mixture of 100 mM DTT and 25 mM ammonium bicarbonate for 30 min at 56°C. The reaction was subsequently exchanged for the alkylation step with 55 mM iodoacetamide and 25 mM ammonium bicarbonate and incubated in the dark at room temperature for 25 min. The solution was then washed with the 50 mM ammonium bicarbonate and 50% acetonitrile mixture. The gel pieces were then first dehydrated with 100% acetonitrile and then rehydrated with sequence grade trypsin solution (0.6 µg, Promega) and incubated overnight at 37°C. The reaction was quenched with 10 µL of 50% acetonitrile and 0.1% formic acid (FA, Sigma) and transferred to new microfuge tubes, vortexed for 5 min, and centrifuged at 15,000 rpm for 30 min. Samples were transferred to mass spectrometry vials and quantitated by LC-MS as described for peptide identification [69,70]. Peptides were identified as previously described [67] using MassHunter Qualitative Analysis, version 6.0 (Agilent Technologies), Peptide Analysis Worksheet (ProteoMetrics LLC), and PeptideShaker, version 1.16.42, paired with SearchGUI, version 3.3.16 (CompOmics). Crosslinks were then determined using Spectrum Identification Machine (SIMXL 1.5.5.2).

Cy3/Cy5 FRET based steady state ssDNA wrapping experiments

FRET-based analyses of ssDNA binding, and wrapping by full-length Rad52, and $Rad52^{\Delta C}$ proteins was carried out by titrating the protein into ssDNA with Cy5 and Cy3 labels at either ends. A 2 mL of 30 nM solution containing ssDNA (5′-Cy5-$(dT)_{80}$-Cy3-3′) was taken in 50 mM Tris-

Acetate pH 7.5, 50 mM KCl, 5 mM $MgCl_2$, 10% v/v glycerol, 1 mM DTT, and 0.2 mg/mL BSA in a 10 mm pathlength quartz cuvette in ISS spectrofluorometer. The temperature was maintained at 23°C constant stirring. The samples were taken in triplicate, excited with 535 nm light, and the resulting emission from the donor (Cy3), and the sensitized emission from the acceptor (Cy5) was collected as a FRET scan from 550 – 700 nm. FRET efficiency was calculated from background subtracted FRET spectra as follows:

$$FRET_e = \frac{I_A}{I_A + I_D} \quad \ldots. (4)$$

Where $FRET_e$ is the FRET efficiency calculated by normalizing the sensitized emission counts (I_A; fluorescence intensity collected at 667 nm) with total number of photons collected in the donor and the acceptor channel ($I_A + I_D$; fluorescence intensity counts 667 nm + that collected at 568 nm).

No attempt was made to ascertain correction factors for spectral cross-stalk (i.e. Cy3 emission spilling over into Cy5 channel or *vice versa*, or cross-excitation (i.e. 535 nm excitation light directly exciting Cy5 fluorophores) because following two reasons: 1) Equation (4) is a simple means to estimate ratiometric FRET. We are merely interested in monitoring the relative changes in the distance between the ends of the ssDNA upon around Rad52 rather than any precise value, 2) A complete battery of correction factors will also include the proximity-based effects of proximity of the bound protein molecule on the quantum efficiency of Cy3 and Cy5 fluorescence. This will involve additional experiments with Cy3- or Cy5- alone labelled ssDNA of comparable lengths something which is beyond the scope of this present study and unnecessary.

After an initial FRET scan of ssDNA alone, full length Rad52 or $Rad52^{\Delta C}$ were titrated in multiple steps gradually increasing the protein concentration. After each addition, FRET spectra were recollectedwere reacquired after an incubation period of 2′ allowing the binding reaction to come to an equilibrium. The estimated $FRET_e$ was plotted against the concentration of Rad52 in decamer units (see supplementary figure 15) for ssDNA of different lengths. $(dT)_{xx}$, where xx refers to 45, 60, 80 or 97 base ssDNA lengths.

Single-molecule ssDNA-Rad52 wrapping experiments

Single-molecule FRET measurements were performed on an inverted, objective based total-internal-reflection fluorescence microscope (TIR-FM; Olympus Cell-TIRF). TIR excitation was achieved through an oil-immersion objective (100X Olympus UplanApo Numerical Aperture 1.5). The sample was excited with a 532nm laser,532 nm laser and the emitted fluorescence was split into two channels using Optosplit II (Cairn-Research, UK); Cy3 and Cy5 emissions was collected on the half chip of the same electron-multiplying charge-coupled device (EM-CCD) camera (iXon Ultra DU-897U-CS0). Images were acquired with 150 ms frame time. Donor and Acceptor images were subpixel registered in Fiji using an image of multicolor beads as fiducial markers. Next, background corrected intensity traces were extracted from single-molecule spots using Matlab. FRET values were calculated for each fluorescent spot as a function of time as a ratio between the acceptor intensity and the sum of the intensities of the donor and acceptor, corrected for cross-talk and cross-excitation. The single-molecule intensity traces were further analyzed in vbFRET to ascribe FRET states, and dwell times.

Glass coverslips for single-molecule imaging were cleaned and coated as follows: Briefly No. 1.5 thickness Gold Seal coverslips (22 x 60 x 0.17) were sonicated in (1) Deionized Water, (2) 2% Micro-90, (3) 200-proof ethanol, and finally in (4) 1N KOH all at 60°C for 15 minutes each

interspersed with exhaustive washes with deionized water. After drying under a stream of filtered N_2, the coverslips were first coated with Vectabond (1% v/v Vectabond in 1:18 Methanol/Acetic acid mixture) followed by washes with deionized water. Next dried coverslips were incubated overnight with a freshly prepared 18:1 mixture of mPEG-SVA and Biotin-PEG-SVA in 0.1 M $NaHCO_3$. Nonspecific binding, which was measured by flowing in non-biotinylated Cy3- or Cy5-labelled DNA or by flowing in Biotinylated fluorescent DNA substrate in absence of Neutravidin, was <1-2 %. All measurements were performed at room temperature (21 ^oC) in a 50 mM Tris-Acetate pH 7.5, 50 mM KCl, 5 mM $MgCl_2$, 10% v/v glycerol, 1 mM DTT, and 0.2 mg/mL BSA supplemented with oxygen scavenging solution i.e. 0.1 mg/mL glucose oxidase, 02 mg/mL catalase, and 0.4% (wt/wt) β-d-glucose (or 0.1 μM PCD / 10 mM PCA), and 2.5 mM Trolox to reduce single-molecule blinking events.

To a Neutravidin (0.2 mg/mL) coated slide, biotin tagged partial duplexes (18bp18 duplex region) with 3′ dT overhangs and Cy3/Cy5 pairs (see supplementary table 3 for) were added at 50-100 pM concentration to arrive at optimal single-molecule number- density of ~1.2 spot per 3.5 μm^2 area on the EM-CCD chip. Basal FRET (w/o any protein) trajectory was recorded for 5 minutes. Following which 0.9-1.3 nM full-length Rad52 or Rad52$^{\Delta C}$ was introduced. After a 2-3 minute incubation period to re-achieve anoxic conditions and the Rad52-ssDNA binding to arrive at an equilibrium, 5 min long videos were again recorded from the same field of view.

Steady-State ssDNA-Rad52 binding and Rad51 handoff experiments

To 30 nM ssDNA (5′-Cy5-$(dT)_{80}$-Cy3-3′) taken in 50 mM Tris-Acetate pH 7.5, 50 mM KCl, 5 mM $MgCl_2$, 10% v/v glycerol, 1 mM DTT, and 0.2 mg/mL BSA in a 10 mm path-length cuvette full length Rad52 or Rad52$^{\Delta C}$ was added until the FRET peaked indicating the end of binding reaction. Next, increasing concentration of Rad51 ($\pm$2.5 mM ATP) was added to the reaction in stepwise manner. As Rad51 concentration was increased, average FRET begins to decrease especially in the case where ATP was present in the reaction. These results are consistent with the model that bound and polymerizing Rad51 can pull DNA after binding, the ATP-dependent polymerization of Rad51 extracts ssDNA away from Rad52-wrapped configuration linearizing it.

Stopped Flow analysis of DNA binding and Rad51 filament formation

Stopped-flow experiments were performed using an Applied Photophysics SX20 instrument (Applied Photophysics Inc.) at 25°C in reaction buffer (50mM Tris-Acetate pH 7.5, 5mM $MgCl_2$, 10% glycerol, 1mM DTT). Reactions from individual syringes were rapidly mixed and fluorescence data were collected. The respective mixing schemes are denoted by cartoon schematics within the figure panel. Five individual shots were averaged for each experiment. All experiments were repeated a minimum of 3 times. In FRET experiments, samples were excited at 535 nm and Cy5 emission was captured using a 645 nm band-pass filter. For the Cy3-$dT_{(80)}$-Cy5 Rad52-Rad51 interactions, Rad52-DNA and Rad52-DNA-Rad51DNARad51 interactions, experiments were performed with 100 nM each of, Rad52 (decamer) Rad51, and Cy3-$dT_{(80)}$-Cy5 ssDNA substrates (1:1:1 ratio).

References

1 Symington, L. S., Rothstein, R. & Lisby, M. Mechanisms and regulation of mitotic recombination in Saccharomyces cerevisiae. *Genetics* **198**, 795-835, doi:10.1534/genetics.114.166140 (2014).

2 Sung, P. & Klein, H. Mechanism of homologous recombination: mediators and helicases take on regulatory functions. *Nat Rev Mol Cell Biol* **7**, 739-750, doi:10.1038/nrm2008 (2006).

3 Symington, L. S. Role of RAD52 epistasis group genes in homologous recombination and double-strand break repair. *Microbiol Mol Biol Rev* **66**, 630-670, table of contents, doi:10.1128/MMBR.66.4.630-670.2002 (2002).

4 van Gent, D. C., Hoeijmakers, J. H. & Kanaar, R. Chromosomal stability and the DNA double-stranded break connection. *Nat Rev Genet* **2**, 196-206, doi:10.1038/35056049 (2001).

5 Stewart, M. D. *et al.* Homologous Recombination Deficiency: Concepts, Definitions, and Assays. *Oncologist* **27**, 167-174, doi:10.1093/oncolo/oyab053 (2022).

6 Marechal, A. & Zou, L. RPA-coated single-stranded DNA as a platform for post-translational modifications in the DNA damage response. *Cell Res* **25**, 9-23, doi:10.1038/cr.2014.147 (2015).

7 Wold, M. S. Replication protein A: a heterotrimeric, single-stranded DNA-binding protein required for eukaryotic DNA metabolism. *Annu Rev Biochem* **66**, 61-92, doi:10.1146/annurev.biochem.66.1.61 (1997).

8 Deshpande, I. *et al.* Structural Basis of Mec1-Ddc2-RPA Assembly and Activation on Single-Stranded DNA at Sites of Damage. *Mol Cell* **68**, 431-445 e435, doi:10.1016/j.molcel.2017.09.019 (2017).

9 Navadgi-Patil, V. M. & Burgers, P. M. The unstructured C-terminal tail of the 9-1-1 clamp subunit Ddc1 activates Mec1/ATR via two distinct mechanisms. *Mol Cell* **36**, 743-753, doi:10.1016/j.molcel.2009.10.014 (2009).

10 Andriuskevicius, T., Kotenko, O. & Makovets, S. Putting together and taking apart: assembly and disassembly of the Rad51 nucleoprotein filament in DNA repair and genome stability. *Cell Stress* **2**, 96-112, doi:10.15698/cst2018.05.134 (2018).

11 San Filippo, J., Sung, P. & Klein, H. Mechanism of eukaryotic homologous recombination. *Annu Rev Biochem* **77**, 229-257, doi:10.1146/annurev.biochem.77.061306.125255 (2008).

12 Heyer, W. D., Ehmsen, K. T. & Liu, J. Regulation of homologous recombination in eukaryotes. *Annu Rev Genet* **44**, 113-139, doi:10.1146/annurev-genet-051710-150955 (2010).

13 Davies, A. A. *et al.* Role of BRCA2 in control of the RAD51 recombination and DNA repair protein. *Mol Cell* **7**, 273-282, doi:10.1016/s1097-2765(01)00175-7 (2001).

14 Paques, F. & Haber, J. E. Multiple pathways of recombination induced by double-strand breaks in Saccharomyces cerevisiae. *Microbiol Mol Biol Rev* **63**, 349-404, doi:10.1128/MMBR.63.2.349-404.1999 (1999).

15 Mortensen, U. H., Bendixen, C., Sunjevaric, I. & Rothstein, R. DNA strand annealing is promoted by the yeast Rad52 protein. *Proc Natl Acad Sci U S A* **93**, 10729-10734, doi:10.1073/pnas.93.20.10729 (1996).

16 Prado, F., Cortes-Ledesma, F., Huertas, P. & Aguilera, A. Mitotic recombination in Saccharomyces cerevisiae. *Curr Genet* **42**, 185-198, doi:10.1007/s00294-002-0346-3 (2003).

17 Davis, A. P. & Symington, L. S. RAD51-dependent break-induced replication in yeast. *Mol Cell Biol* **24**, 2344-2351, doi:10.1128/MCB.24.6.2344-2351.2004 (2004).

18 Bartsch, S., Kang, L. E. & Symington, L. S. RAD51 is required for the repair of plasmid double-stranded DNA gaps from either plasmid or chromosomal templates. *Mol Cell Biol* **20**, 1194-1205, doi:10.1128/MCB.20.4.1194-1205.2000 (2000).
19 Stasiak, A. Z. *et al.* The human Rad52 protein exists as a heptameric ring. *Curr Biol* **10**, 337-340, doi:10.1016/s0960-9822(00)00385-7 (2000).
20 Grimme, J. M. *et al.* Human Rad52 binds and wraps single-stranded DNA and mediates annealing via two hRad52-ssDNA complexes. *Nucleic Acids Res* **38**, 2917-2930, doi:10.1093/nar/gkp1249 (2010).
21 Shinohara, A., Shinohara, M., Ohta, T., Matsuda, S. & Ogawa, T. Rad52 forms ring structures and co-operates with RPA in single-strand DNA annealing. *Genes Cells* **3**, 145-156, doi:10.1046/j.1365-2443.1998.00176.x (1998).
22 Kagawa, W. *et al.* Functional analyses of the C-terminal half of the Saccharomyces cerevisiae Rad52 protein. *Nucleic Acids Res* **42**, 941-951, doi:10.1093/nar/gkt986 (2014).
23 Singleton, M. R., Wentzell, L. M., Liu, Y., West, S. C. & Wigley, D. B. Structure of the single-strand annealing domain of human RAD52 protein. *Proc Natl Acad Sci U S A* **99**, 13492-13497, doi:10.1073/pnas.212449899 (2002).
24 Kagawa, W. *et al.* Crystal structure of the homologous-pairing domain from the human Rad52 recombinase in the undecameric form. *Mol Cell* **10**, 359-371, doi:10.1016/s1097-2765(02)00587-7 (2002).
25 Welty, S. *et al.* RAD52 is required for RNA-templated recombination repair in post-mitotic neurons. *J Biol Chem* **293**, 1353-1362, doi:10.1074/jbc.M117.808402 (2018).
26 McDevitt, S., Rusanov, T., Kent, T., Chandramouly, G. & Pomerantz, R. T. How RNA transcripts coordinate DNA recombination and repair. *Nat Commun* **9**, 1091, doi:10.1038/s41467-018-03483-7 (2018).
27 Mazina, O. M., Keskin, H., Hanamshet, K., Storici, F. & Mazin, A. V. Rad52 Inverse Strand Exchange Drives RNA-Templated DNA Double-Strand Break Repair. *Mol Cell* **67**, 19-29 e13, doi:10.1016/j.molcel.2017.05.019 (2017).
28 Shi, I. *et al.* Role of the Rad52 amino-terminal DNA binding activity in DNA strand capture in homologous recombination. *J Biol Chem* **284**, 33275-33284, doi:10.1074/jbc.M109.057752 (2009).
29 Sugiyama, T., New, J. H. & Kowalczykowski, S. C. DNA annealing by RAD52 protein is stimulated by specific interaction with the complex of replication protein A and single-stranded DNA. *Proc Natl Acad Sci U S A* **95**, 6049-6054, doi:10.1073/pnas.95.11.6049 (1998).
30 Krejci, L. *et al.* Interaction with Rad51 is indispensable for recombination mediator function of Rad52. *J Biol Chem* **277**, 40132-40141, doi:10.1074/jbc.M206511200 (2002).
31 Song, B. & Sung, P. Functional interactions among yeast Rad51 recombinase, Rad52 mediator, and replication protein A in DNA strand exchange. *J Biol Chem* **275**, 15895-15904, doi:10.1074/jbc.M910244199 (2000).
32 Deng, X. *et al.* Human replication protein A-Rad52-single-stranded DNA complex: stoichiometry and evidence for strand transfer regulation by phosphorylation. *Biochemistry* **48**, 6633-6643, doi:10.1021/bi900564k (2009).
33 Plate, I. *et al.* Interaction with RPA is necessary for Rad52 repair center formation and for its mediator activity. *J Biol Chem* **283**, 29077-29085, doi:10.1074/jbc.M804881200 (2008).
34 Park, M. S., Ludwig, D. L., Stigger, E. & Lee, S. H. Physical interaction between human RAD52 and RPA is required for homologous recombination in mammalian cells. *J Biol Chem* **271**, 18996-19000, doi:10.1074/jbc.271.31.18996 (1996).

35 Khade, N. V. & Sugiyama, T. Roles of C-Terminal Region of Yeast and Human Rad52 in Rad51-Nucleoprotein Filament Formation and ssDNA Annealing. *PLoS One* **11**, e0158436, doi:10.1371/journal.pone.0158436 (2016).
36 Seong, C. *et al.* Molecular anatomy of the recombination mediator function of Saccharomyces cerevisiae Rad52. *J Biol Chem* **283**, 12166-12174, doi:10.1074/jbc.M800763200 (2008).
37 Saotome, M. *et al.* Structural Basis of Homology-Directed DNA Repair Mediated by RAD52. *iScience* **3**, 50-62, doi:10.1016/j.isci.2018.04.005 (2018).
38 Arai, N. *et al.* Vital roles of the second DNA-binding site of Rad52 protein in yeast homologous recombination. *J Biol Chem* **286**, 17607-17617, doi:10.1074/jbc.M110.216739 (2011).
39 Kagawa, W. *et al.* Identification of a second DNA binding site in the human Rad52 protein. *J Biol Chem* **283**, 24264-24273, doi:10.1074/jbc.M802204200 (2008).
40 Oshidari, R. *et al.* DNA repair by Rad52 liquid droplets. *Nat Commun* **11**, 695, doi:10.1038/s41467-020-14546-z (2020).
41 Yan, Z. *et al.* Rad52 Restrains Resection at DNA Double-Strand Break Ends in Yeast. *Mol Cell* **76**, 699-711 e696, doi:10.1016/j.molcel.2019.08.017 (2019).
42 Li, F. *et al.* Identification of an integrase-independent pathway of retrotransposition. *Sci Adv* **8**, eabm9390, doi:10.1126/sciadv.abm9390 (2022).
43 Paulsen, B. S. *et al.* Ectopic expression of RAD52 and dn53BP1 improves homology-directed repair during CRISPR-Cas9 genome editing. *Nat Biomed Eng* **1**, 878-888, doi:10.1038/s41551-017-0145-2 (2017).
44 Xu, Y., Zhou, H., Post, G., Zan, H. & Casali, P. Rad52 mediates class-switch DNA recombination to IgD. *Nat Commun* **13**, 980, doi:10.1038/s41467-022-28576-2 (2022).
45 Tokmina-Lukaszewska, M. *et al.* The Role of Mass Spectrometry in Structural Studies of Flavin-Based Electron Bifurcating Enzymes. *Front Microbiol* **9**, 1397, doi:10.3389/fmicb.2018.01397 (2018).
46 Gong, Z., Ye, S. X. & Tang, C. Tightening the Crosslinking Distance Restraints for Better Resolution of Protein Structure and Dynamics. *Structure* **28**, 1160-1167 e1163, doi:10.1016/j.str.2020.07.010 (2020).
47 Ma, E. *et al.* Rad52-Rad51 association is essential to protect Rad51 filaments against Srs2, but facultative for filament formation. *Elife* **7**, doi:10.7554/eLife.32744 (2018).
48 Antony, E. *et al.* Srs2 disassembles Rad51 filaments by a protein-protein interaction triggering ATP turnover and dissociation of Rad51 from DNA. *Mol Cell* **35**, 105-115, doi:10.1016/j.molcel.2009.05.026 (2009).
49 New, J. H., Sugiyama, T., Zaitseva, E. & Kowalczykowski, S. C. Rad52 protein stimulates DNA strand exchange by Rad51 and replication protein A. *Nature* **391**, 407-410, doi:10.1038/34950 (1998).
50 Sugiyama, T. & Kowalczykowski, S. C. Rad52 protein associates with replication protein A (RPA)-single-stranded DNA to accelerate Rad51-mediated displacement of RPA and presynaptic complex formation. *J Biol Chem* **277**, 31663-31672, doi:10.1074/jbc.M203494200 (2002).
51 Gibb, B. *et al.* Protein dynamics during presynaptic-complex assembly on individual single-stranded DNA molecules. *Nat Struct Mol Biol* **21**, 893-900, doi:10.1038/nsmb.2886 (2014).
52 Saotome, M., Saito, K., Onodera, K., Kurumizaka, H. & Kagawa, W. Structure of the human DNA-repair protein RAD52 containing surface mutations. *Acta Crystallogr F Struct Biol Commun* **72**, 598-603, doi:10.1107/S2053230X1601027X (2016).
53 Sugawara, N., Wang, X. & Haber, J. E. In vivo roles of Rad52, Rad54, and Rad55 proteins in Rad51-mediated recombination. *Mol Cell* **12**, 209-219, doi:10.1016/s1097-2765(03)00269-7 (2003).

54 Sung, P. Function of yeast Rad52 protein as a mediator between replication protein A and the Rad51 recombinase. *J Biol Chem* **272**, 28194-28197, doi:10.1074/jbc.272.45.28194 (1997).
55 Jaffe, E., Bornstein, P. & Disteche, C. M. Mapping of the thrombospondin gene to human chromosome 15 and mouse chromosome 2 by in situ hybridization. *Genomics* **7**, 123-126, doi:10.1016/0888-7543(90)90528-3 (1990).
56 Greene, E. C. DNA Sequence Alignment during Homologous Recombination. *J Biol Chem* **291**, 11572-11580, doi:10.1074/jbc.R116.724807 (2016).
57 Qi, Z. *et al.* DNA sequence alignment by microhomology sampling during homologous recombination. *Cell* **160**, 856-869, doi:10.1016/j.cell.2015.01.029 (2015).
58 Lee, J. Y. *et al.* DNA RECOMBINATION. Base triplet stepping by the Rad51/RecA family of recombinases. *Science* **349**, 977-981, doi:10.1126/science.aab2666 (2015).
59 Ragunathan, K., Liu, C. & Ha, T. RecA filament sliding on DNA facilitates homology search. *Elife* **1**, e00067, doi:10.7554/eLife.00067 (2012).
60 Hsieh, P., Camerini-Otero, C. S. & Camerini-Otero, R. D. The synapsis event in the homologous pairing of DNAs: RecA recognizes and pairs less than one helical repeat of DNA. *Proc Natl Acad Sci U S A* **89**, 6492-6496, doi:10.1073/pnas.89.14.6492 (1992).
61 Pokhrel, N. *et al.* Dynamics and selective remodeling of the DNA-binding domains of RPA. *Nat Struct Mol Biol* **26**, 129-136, doi:10.1038/s41594-018-0181-y (2019).
62 Kuppa, S. *et al.* Rtt105 regulates RPA function by configurationally stapling the flexible domains. *Nat Commun* **13**, 5152, doi:10.1038/s41467-022-32860-6 (2022).
63 Schuck, P. Size-distribution analysis of macromolecules by sedimentation velocity ultracentrifugation and lamm equation modeling. *Biophys J* **78**, 1606-1619, doi:10.1016/S0006-3495(00)76713-0 (2000).
64 Punjani, A., Rubinstein, J. L., Fleet, D. J. & Brubaker, M. A. cryoSPARC: algorithms for rapid unsupervised cryo-EM structure determination. *Nat Methods* **14**, 290-296, doi:10.1038/nmeth.4169 (2017).
65 Pettersen, E. F. *et al.* UCSF ChimeraX: Structure visualization for researchers, educators, and developers. *Protein Sci* **30**, 70-82, doi:10.1002/pro.3943 (2021).
66 Patterson, A., Zhao, Z., Waymire, E., Zlotnick, A. & Bothner, B. Dynamics of Hepatitis B Virus Capsid Protein Dimer Regulate Assembly through an Allosteric Network. *ACS Chem Biol* **15**, 2273-2280, doi:10.1021/acschembio.0c00481 (2020).
67 Berry, L., Patterson, A., Pence, N., Peters, J. W. & Bothner, B. Hydrogen Deuterium Exchange Mass Spectrometry of Oxygen Sensitive Proteins. *Bio Protoc* **8**, doi:10.21769/BioProtoc.2769 (2018).
68 Kavan, D. a. M., P. MSTools—Web based application for visualization and presentation of HXMS data. *International Journal of Mass Spectrometry* **302**, 53-58 (2010).
69 Burns, E. E., Keith, B. K., Refai, M. Y., Bothner, B. & Dyer, W. E. Proteomic and biochemical assays of glutathione-related proteins in susceptible and multiple herbicide resistant Avena fatua L. *Pestic Biochem Physiol* **140**, 69-78, doi:10.1016/j.pestbp.2017.06.007 (2017).
70 Kim, C. *et al.* Core Protein-Directed Antivirals and Importin beta Can Synergistically Disrupt Hepatitis B Virus Capsids. *J Virol* **96**, e0139521, doi:10.1128/JVI.01395-21 (2022).

Supplementary Information

C-terminus induced asymmetry within a Rad52 homodecamer dictates single-position Rad51 nucleation in homologous recombination

Jaigeeth Deveryshetty[1,§], Rahul Chadda[1,§], Jenna Mattice[2], Simrithaa Karunakaran[1], Michael J. Rau[3], Katherine Basore[3] Nilisha Pokhrel[4], Noah Englander[1], James A.J. Fitzpatrick[3], Brian Bothner[2] and Edwin Antony[1,*]

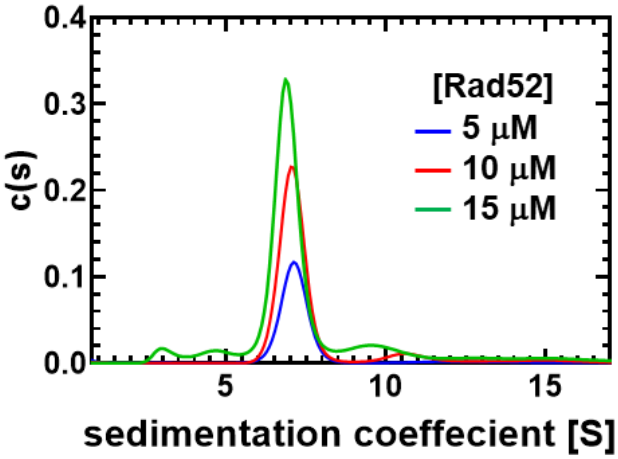

Supplementary Figure 1. *Saccharomyces cerevisiae* Rad52 is predominantly a single species solution. Sedimentation velocity analytical ultracentrifugation (AUC^{SV}) analysis of full-length *S. cerevisiae* Rad52 were performed at various concentrations of protein (monomer concentrations noted). Rad52 is predominantly a single species in solution with an estimated molecular mass corresponding to a (please refer to Supplementary Table 2 for measured parameters).

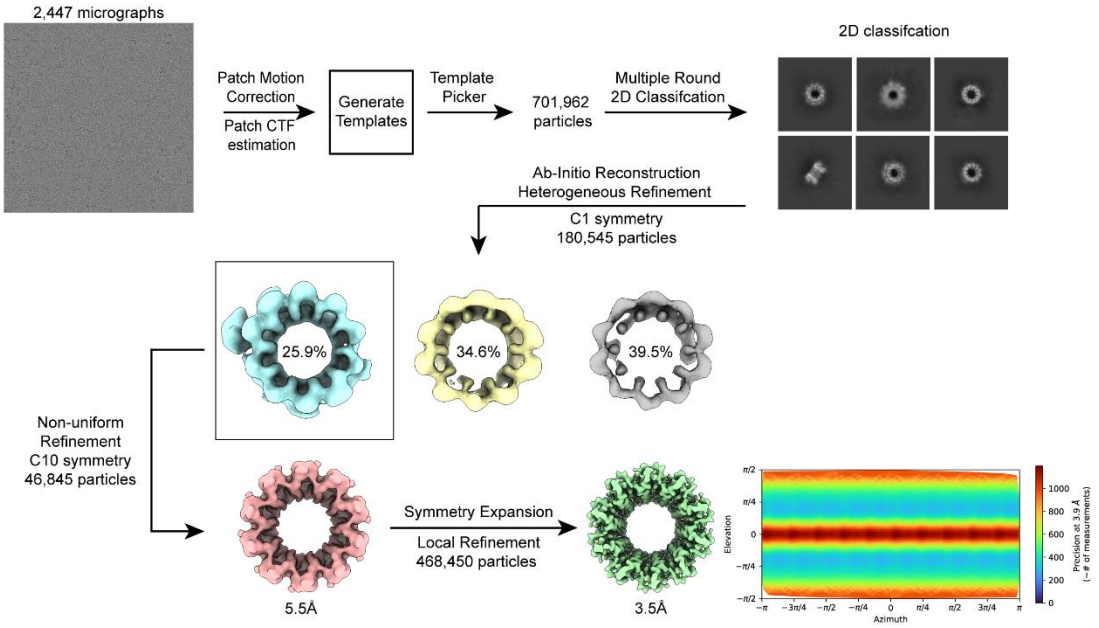

Supplementary Figure 2. Workflow of single particle analysis of the apo Rad52 Cryo-EM data.

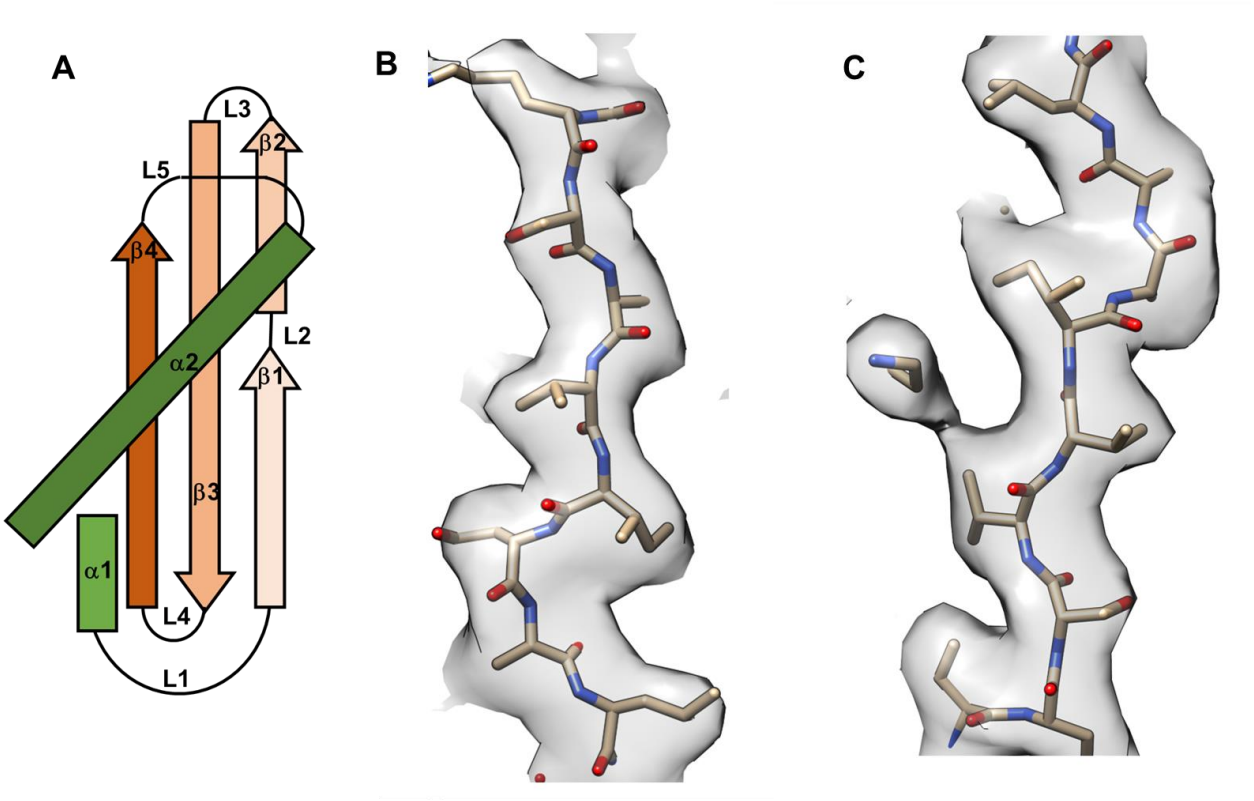

Supplementary Figure 3. Structural details of *S. cerevisiae* Rad52. A) Cartogram of the Rad52 monomer observed in the Cryo-EM structure. **B)** & **C)** Examples of sample maps and models of apo Rad52.

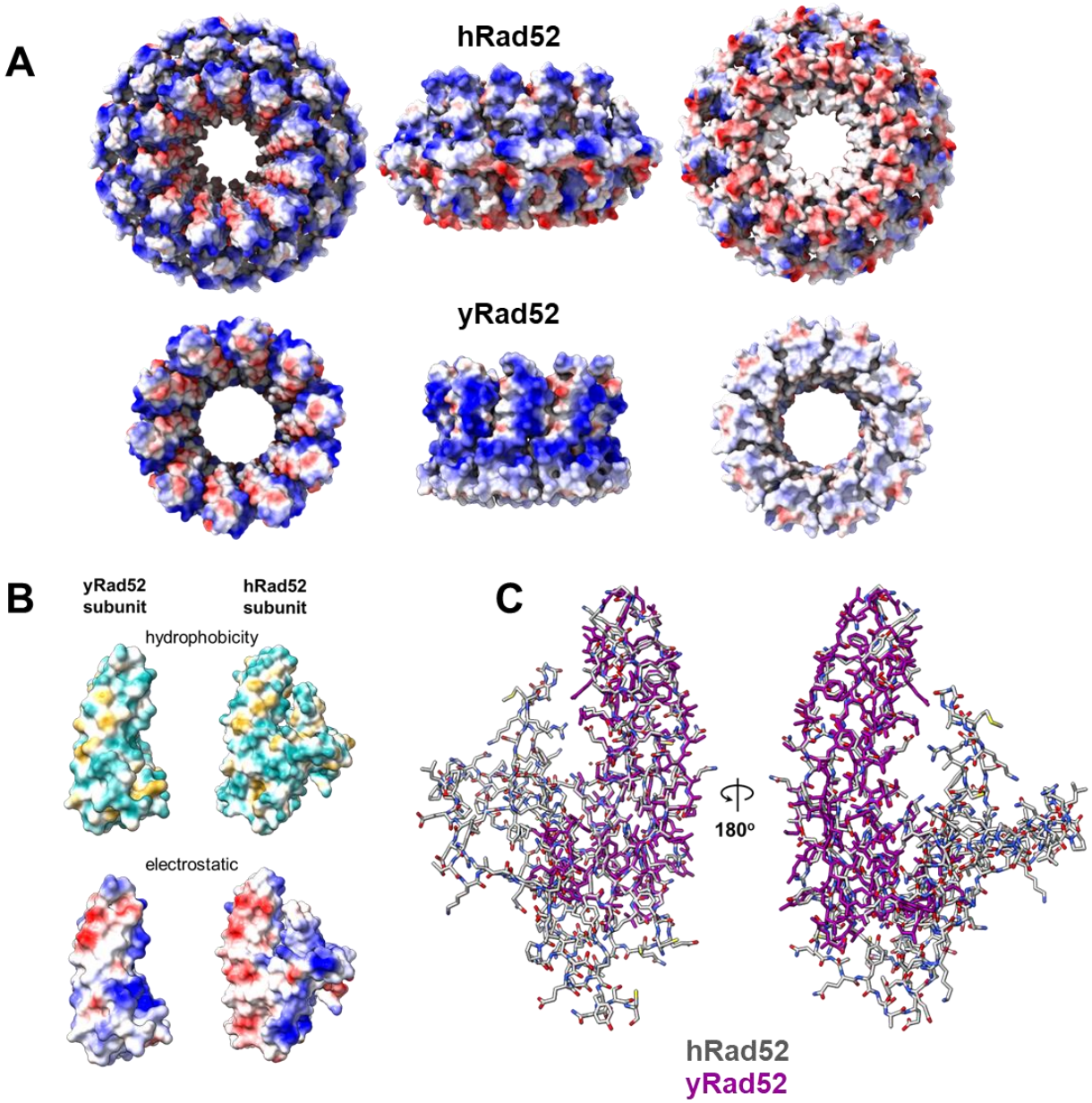

Supplementary Figure 4. Comparison of yeast and human Rad52 structures. A) Electrostatic map of human versus yeast Rad52 showcase the similarity between the two structures. **B)** Electrostatic and hydrophobicity maps of each monomer in the human and yeast Rad52 structures. **C)** Side chain similarity between the human Rad52 and yeast Rad52 structures.

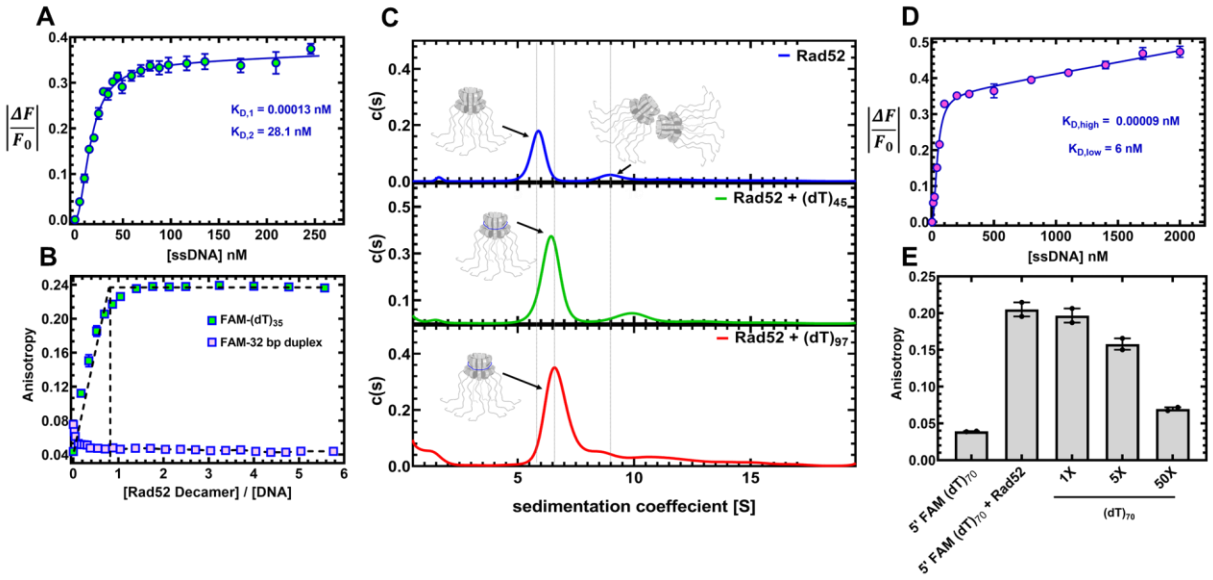

Supplementary Figure 5. Rad52 binds to ssDNA as a homodecamer. A) Intrinsic tryptophan quenching based analysis of ssDNA $(dT)_{84}$ binding to Rad52 shows two binding sites. The data are well described by a high affinity (K_D=1.3x10^{-12}M) and lower affinity binding site (K_D = K_D=28x10^{-9}M) model. **B)** Fluorescence anisotropy measurement of Rad52 binding to a 5′-FAM-$(dT)_{35}$ oligonucleotide shows formation of a stoichiometric complex. Saturation of the lower affinity site is dependent on the length of the DNA. No binding to dsDNA is observed. **C)** Analytical ultracentrifugation analysis of Rad52 in the absence or presence of short [$(dT)_{45}$] or longer [$(dT)_{97}$] ssDNA substrates predominantly show a decamer forming 1:1 complex with DNA. The double decamer species is also capable of binding to ssDNA. **D)** Investigation of the Trp quenching of Rad52 at higher ssDNA concentrations shows additional signal changes. Since Rad52 functions as a single decamer, these data suggest that ssDNA is not uniformly bound around the ring and can likely be looped out between the subunits. **E)** Anisotropy experiments were performed by preforming a Rad52-FAM$(dT)_{70}$ complex and challenged with increasing amounts of unlabeled $(dT)_{70}$. Data shows that the high-affinity ssDNA bound to Rad52 is in dynamic equilibrium and can be remodeled by high concentrations of free DNA in solution.

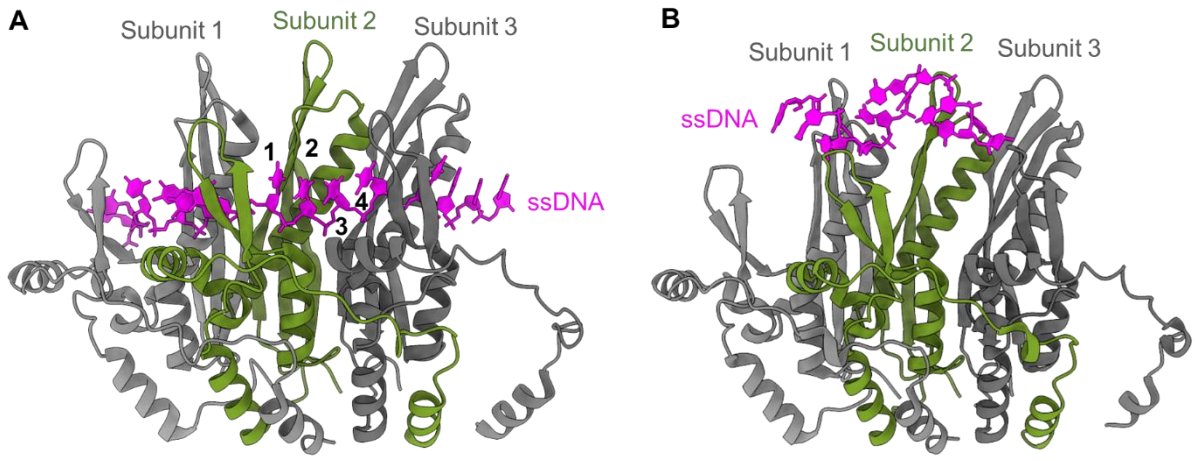

Supplementary Figure 6. Crystal structures of ssDNA bound human Rad52. Three subunits (colored individually) from the undecameric human Rad52 crystal structures are shown. **A)** ssDNA $(dT)_{40}$ bound to the inner binding site was captured when the outer binding site was perturbed by mutating Lys-102 and Lys-133 (PDB ID 5XRZ). **B)** 6nts of a $(dT)_{40}$ ssDNA substrate is observed bound to outer site was captured sandwiched between two Rad52 undecameric rings (PDB ID 5XS0). Shown here are contacts between a single ring and ssDNA.

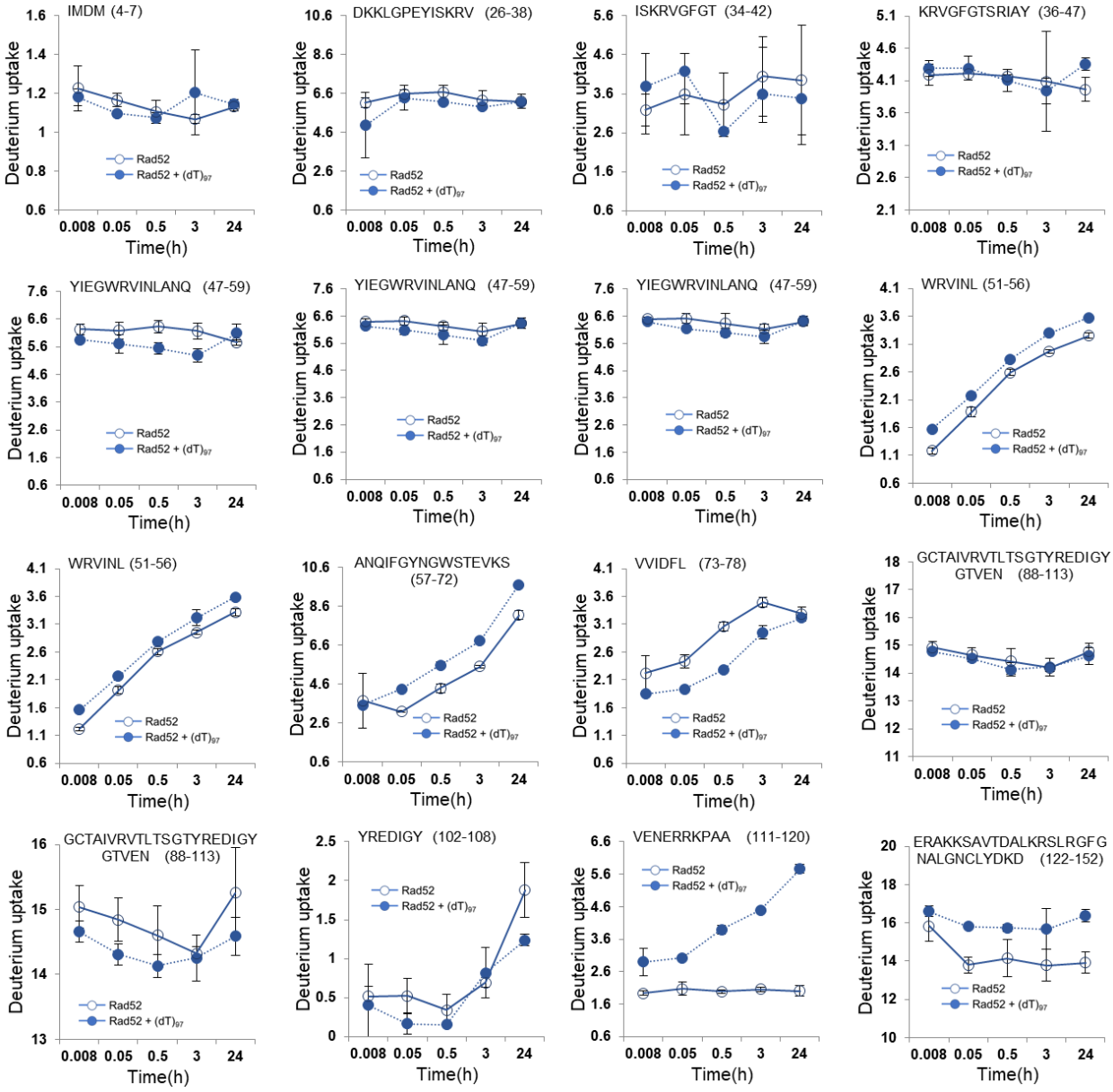

Supplementary Figure 7. Deuterium uptake changes captured in HDX-MS analysis of yeast Rad52. The plotted data for deuterium incorporation as a function of time are shown for individual peptides identified in the HDX-MS analysis. This panel depicts peptides corresponding to amino acid positions 1-152 in the N-terminal half. Data from both Rad52 and the Rad52-$(dT)_{97}$ complex are compared for each peptide.

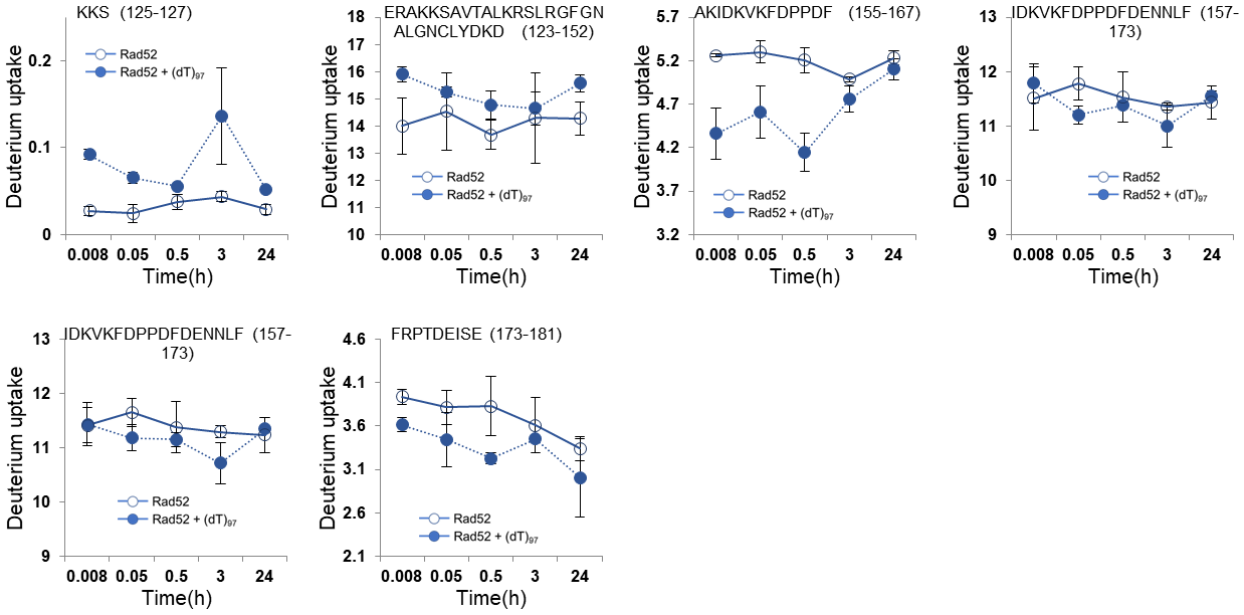

Supplementary Figure 8. Deuterium uptake changes captured in HDX-MS analysis of yeast Rad52. The plotted data for deuterium incorporation as a function of time are shown for individual peptides identified in the HDX-MS analysis. This panel depicts peptides corresponding to amino acid positions 125-181 in the N-terminal half. Data from both Rad52 and the Rad52-$(dT)_{97}$ complex are compared for each peptide.

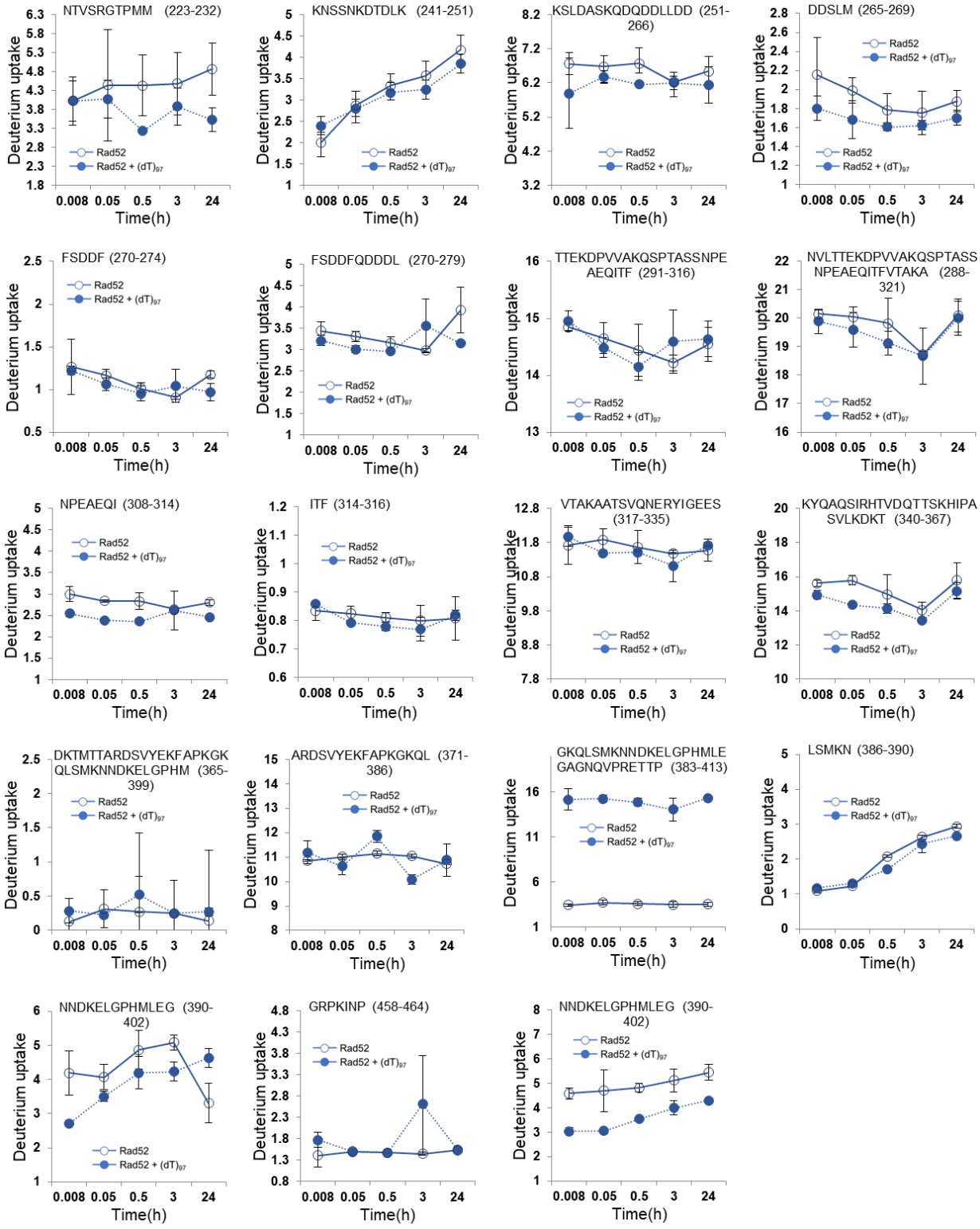

Supplementary Figure 9. Deuterium uptake changes captured in HDX-MS analysis of yeast Rad52. The plotted data for deuterium incorporation as a function of time are shown for individual peptides identified in the HDX-MS analysis. This panel depicts peptides corresponding to amino acid positions 223-464 in the C-terminal half. Data from both Rad52 and the Rad52-$(dT)_{97}$ complex are compared for each peptide.

Supplementary Figure 10. Comparison of the Alphafold model and cryo-EM structure of yeast Rad52. The Alphafold model of *S. cerevisiae* Rad52 (AF-P06778-F1; green) overlaid with the ordered part of the N-terminal half observed in the cryo-EM structure (purple). Excellent agreement in the structures is observed in the N-terminal half between the two.

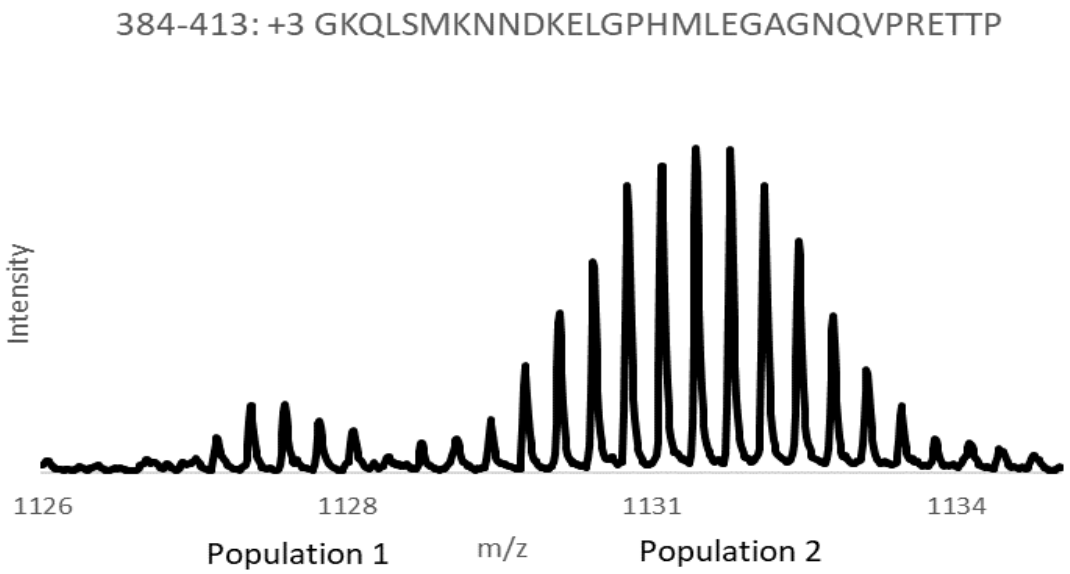

Supplementary Figure 11. Hydrogen/deuterium exchange data of Rad52 peptide 384-413 has a bimodal distribution. Mass spectra of the $(M+3H)^{3+}$ charge state of peptide 384-413 following incubation in 90% deuterium buffer for 30 seconds. Two distinct populations (envelopes) of deuterium uptake were observed. Relative abundance of the different peptide forms is shown in Fig 3E and 3F.

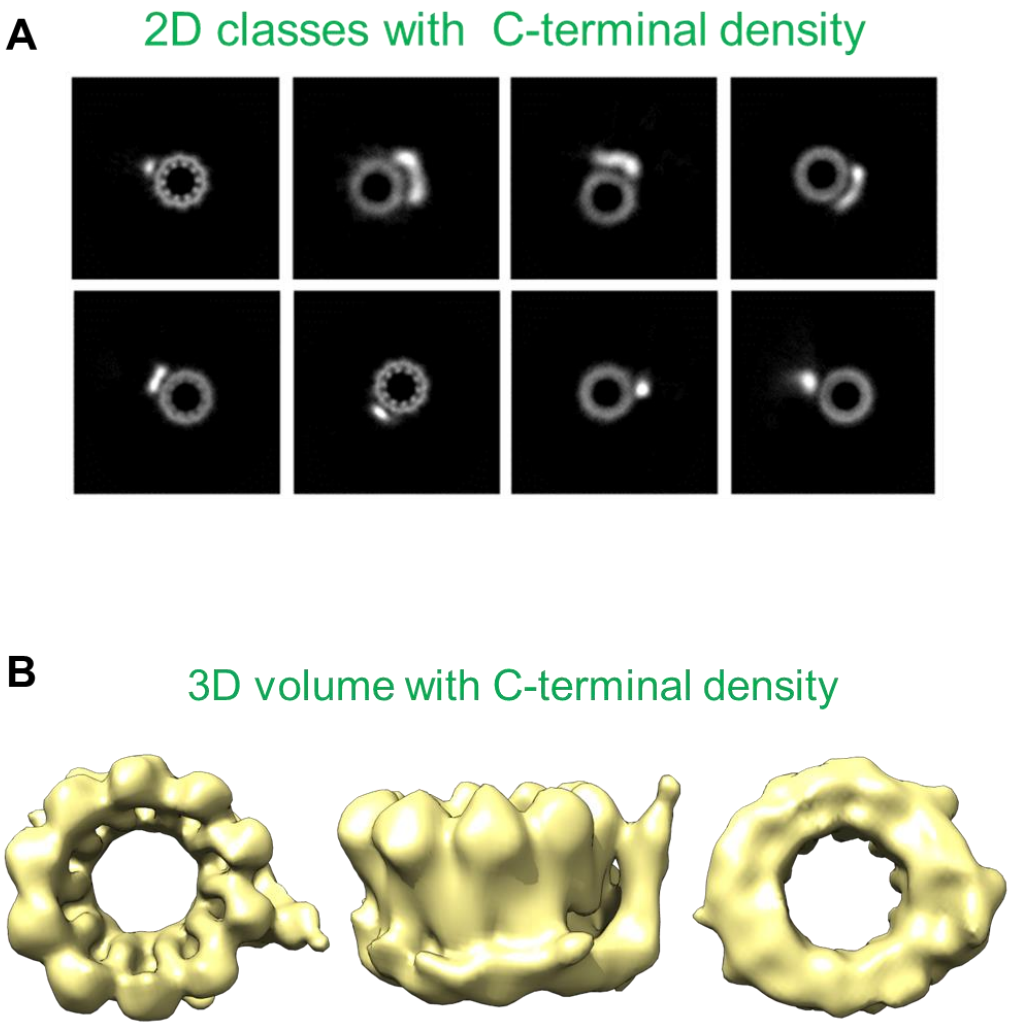

Supplementary Figure 12. Additional density for C-terminal region positioned adjacent to the ordered N-terminal homodecameric ring. A) Examples of 2D classes that are captured in the cryo-EM analysis of Rad52. These classes were discarded in the structure determination, but clearly show presence of additional density adjacent to the ordered N-terminal ring. **B)** Subsequent 3D volumes show that the C-terminal region sits adjacent to the ring but appears to be asymmetrically positioned to one part. The underlying allosteric mechanisms that prevent other subunits in the ring from interacting with their respective C-terminal regions remains to be determined.

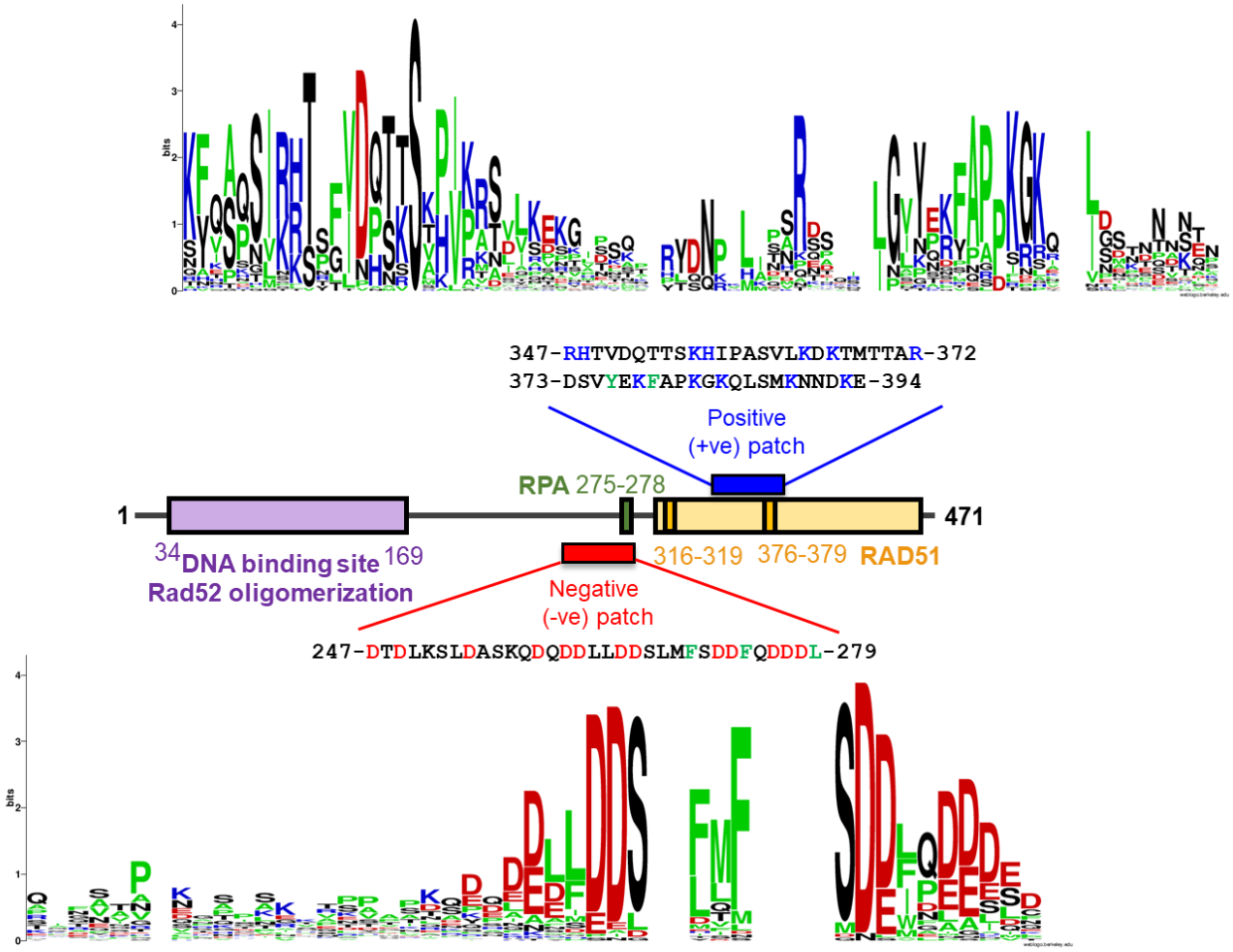

Supplementary Figure 13. Sequence conservation analysis of the C-tail. WebLogo represents sequence similarity analysis of regions in the disordered C-terminal half of Rad52 carrying the Rad51 binding site (positive patch) and the RPA binding site (negative patch). The analysis encompasses Rad52 proteins from 66 different fugal species. Several residues are highly conserved.

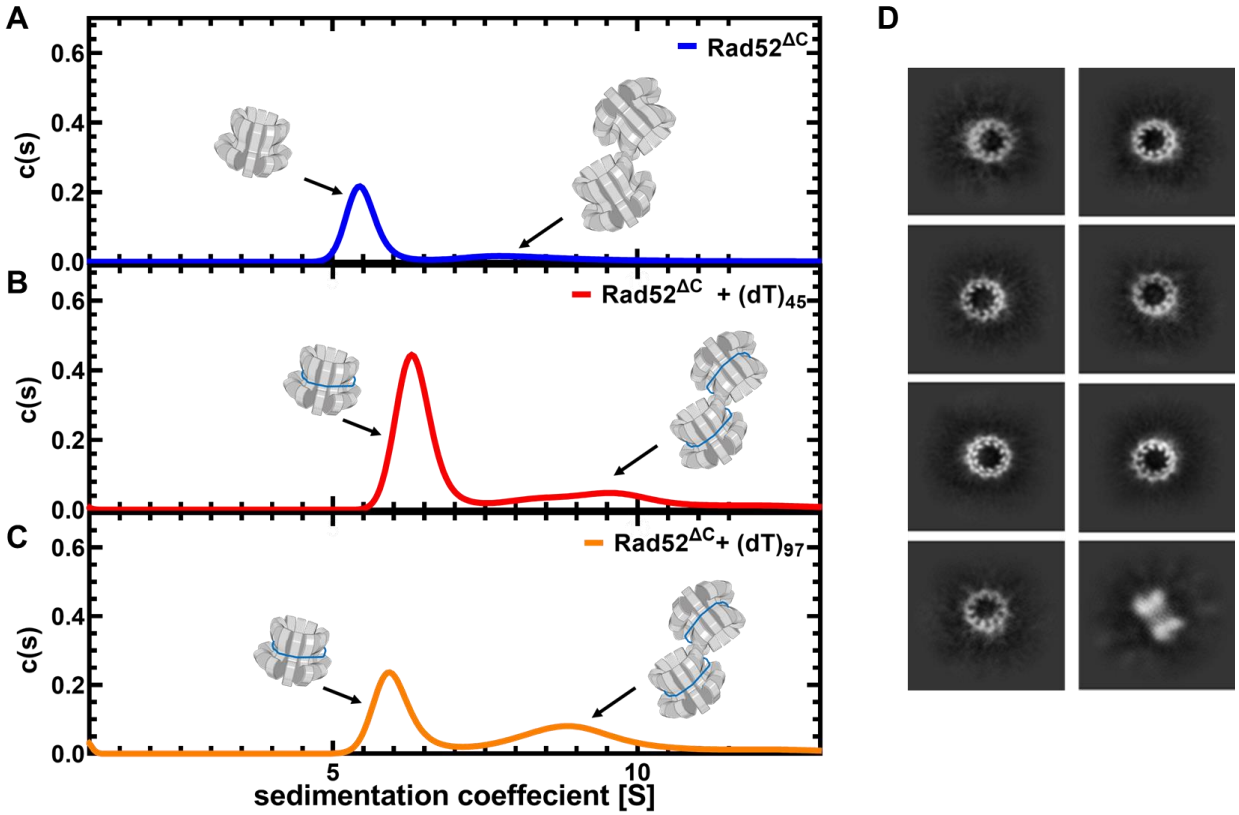

Supplementary Figure 14. Rad52$^{\Delta C}$ is also a homodecamer in solution. Analytical ultracentrifugation sedimentation velocity analysis of **A)** Rad52$^{\Delta C}$ in the absence or presence of **B)** $(dT)_{45}$ or **C)** $(dT)_{97}$ show that the N-terminal half of the protein primarily behaves as a single higher order species corresponding to a homodecamer. A small fraction of the double-ring species is also observed. Both species bind to short and longer ssDNA, however, the species distribution does not change. **D)** 2D classes of Rad52$^{\Delta C}$ in cryo-EM analysis show homodecameric rings.

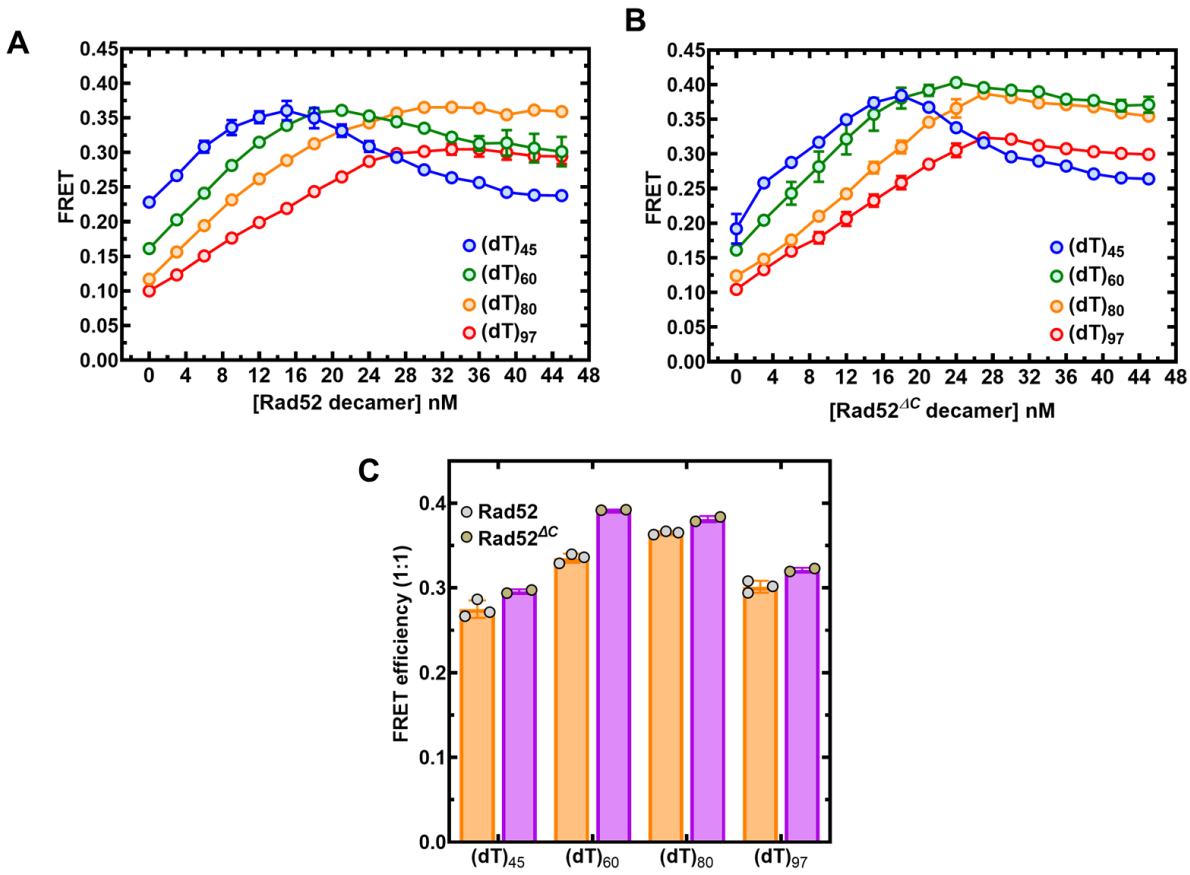

Supplementary Figure 15. ssDNA length dependent change in Rad52 binding induced FRET. ssDNA of varying lengths carrying 5′-Cy5 and 3′-Cy3 fluorophores were subject to **A)** Rad52 or **B)** Rad52$^{\Delta C}$ binding. Changes in FRET were captured by exciting Cy3 and monitoring changes in Cy5 emission. **C)** Optimal FRET for Rad52 is observed on the $(dT)_{80}$ substrate. For Rad52$^{\Delta C}$, highest FRET efficiency is observed on the $(dT)_{60}$ substrate. These data also reveal that the C-tail influences wrapping of the ssDNA around Rad52.

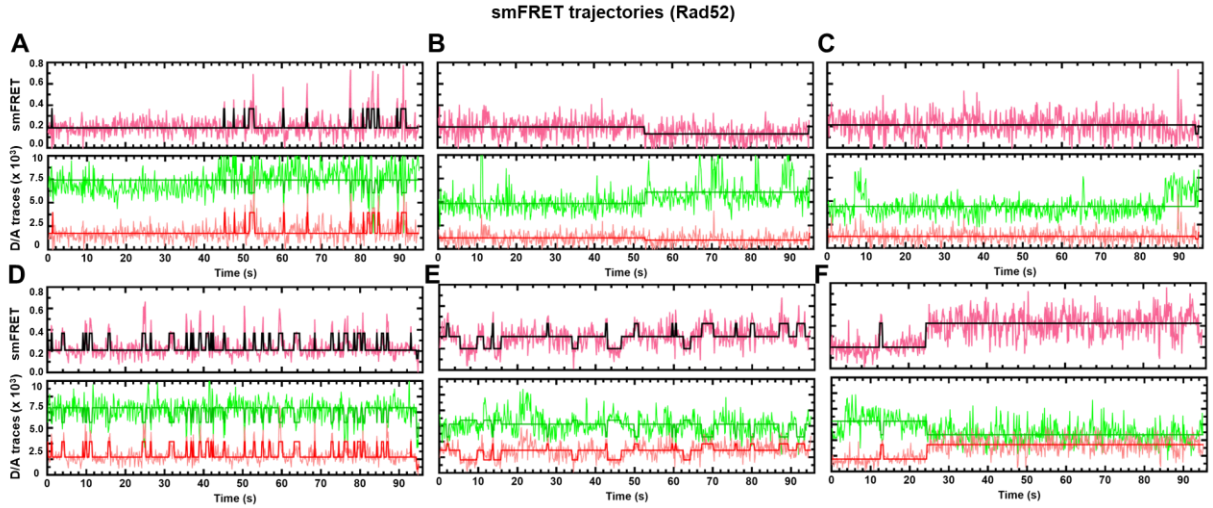

Supplementary Figure 16. Additional single-molecule FRET trajectories for Rad52. Trajectories from six different single DNA molecules are shown from the analysis of full length Rad52.

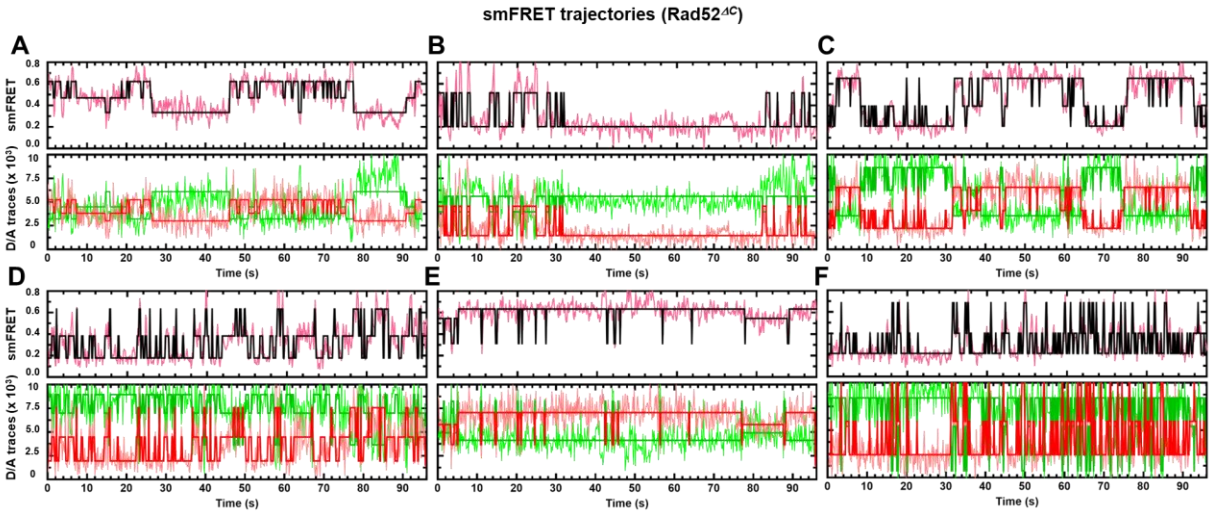

Supplementary Figure 17. Additional single-molecule FRET trajectories for Rad52$^{\Delta C}$. Trajectories from six different single DNA molecules are shown from the analysis of Rad52$^{\Delta C}$.

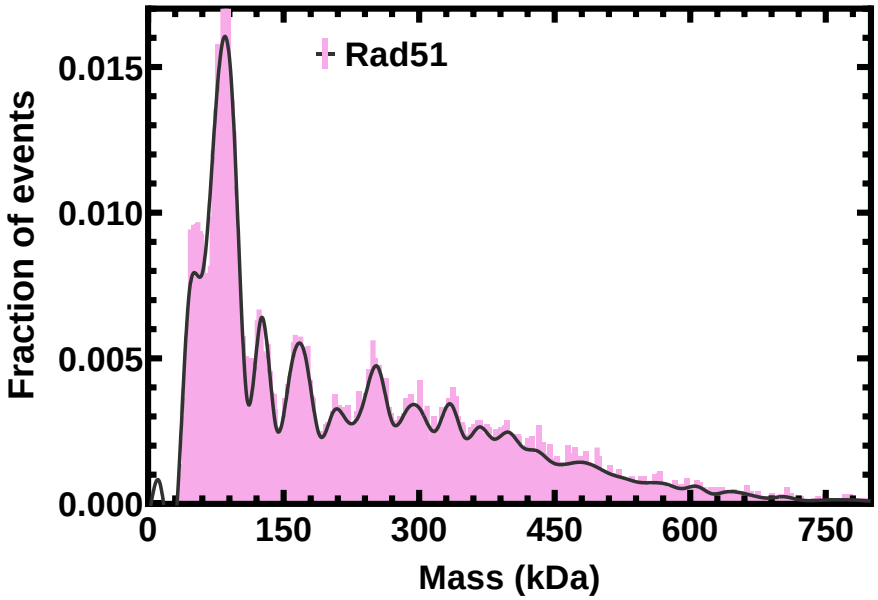

Supplementary Figure 18. Mass photometry analysis of yeast Rad51. Mass photometry analysis of *S. cerevisiae* Rad51 shows the presence of multiple oligomeric species.

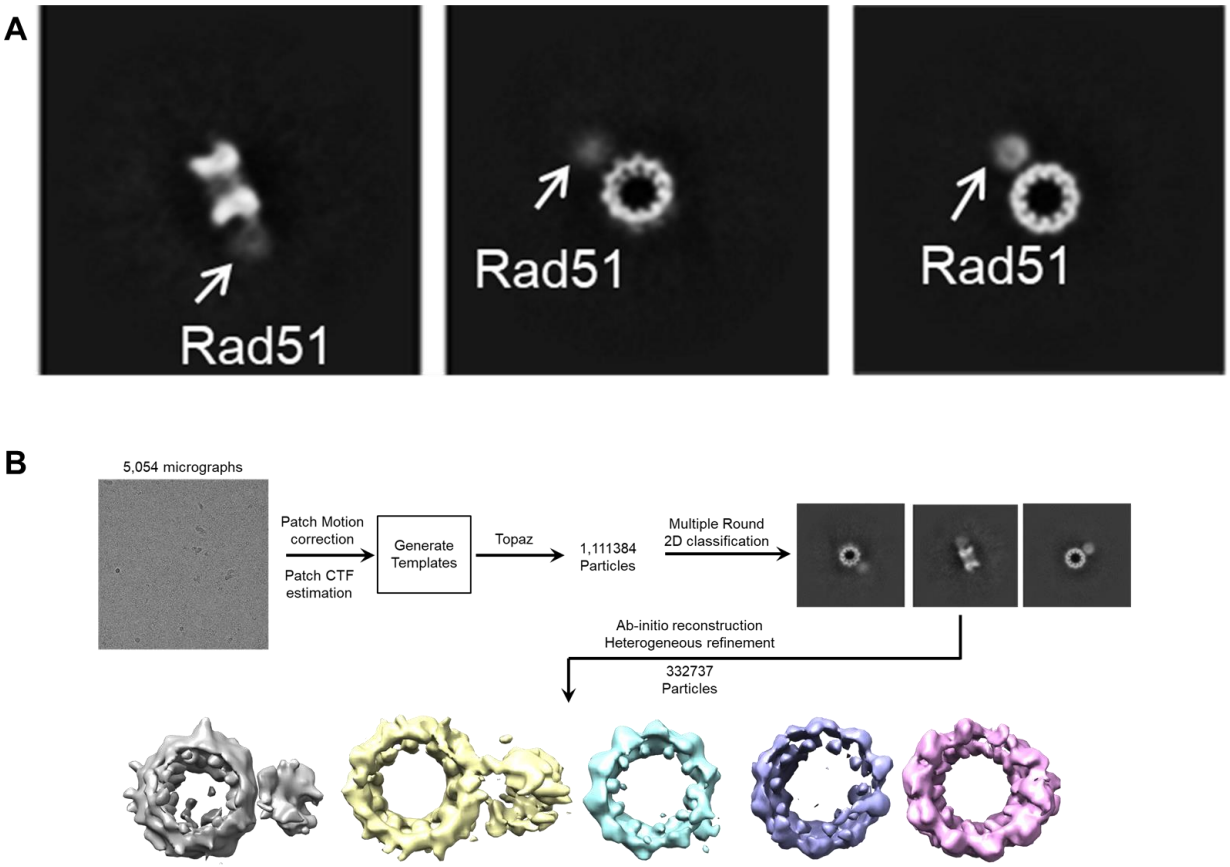

Supplementary Figure 19. Interaction of Rad52-Rad51 complex. A) 2D class averages from the cryo-EM analysis of the Rad51-Rad52 complex are shown. Rad51 molecules are bound to the Rad52 ring, but only at a single defined position. **B)** Workflow of Single particle analysis of Rad52-Rad51 Cryo-EM data

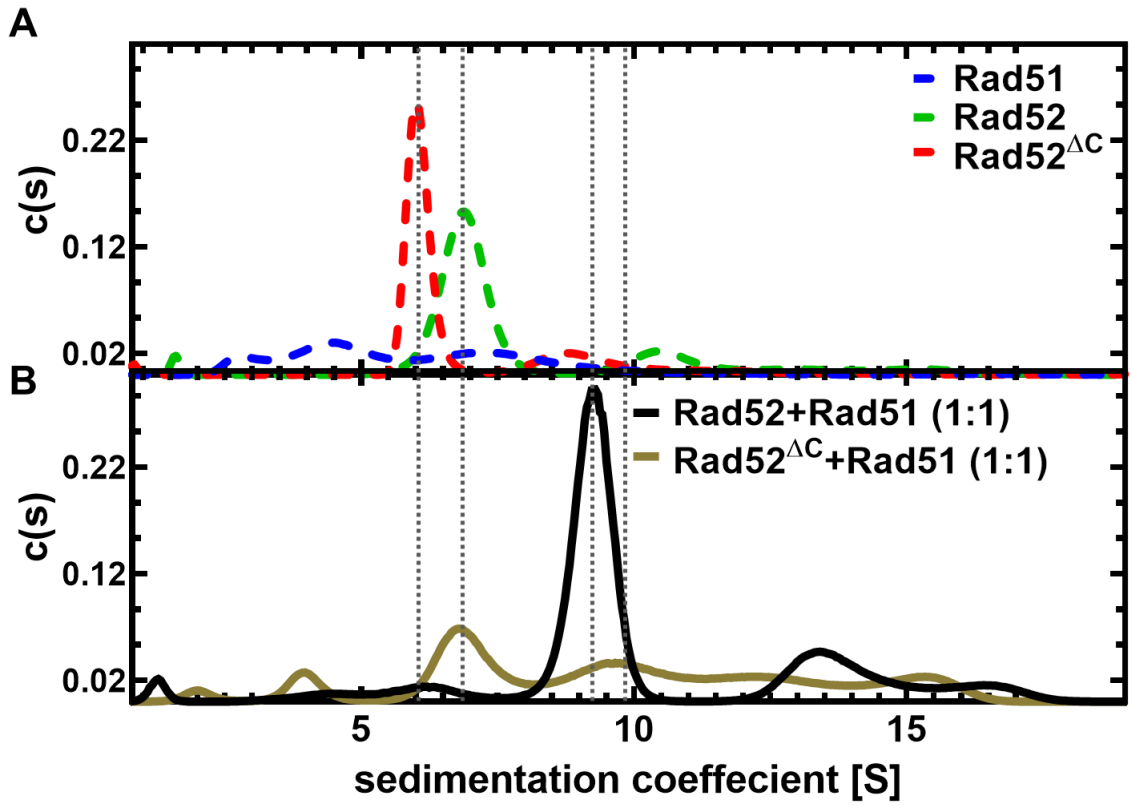

Supplementary Figure 20. Rad52$^{\Delta C}$ displays reduced complex formation with Rad51. Analytical ultracentrifugation sedimentation velocity analysis of **A)** Rad52 (10µM monomer) and Rad52$^{\Delta C}$ (10µM monomer) show the homodimeric versions predominantly behaving as a single species in solution. Rad51 (10 µM monomer) behaves polydisperse with a wide assortment of oligomers. **B)** The sedimentation profiles of Rad52+Rad51 and Rad52$^{\Delta C}$+Rad51 (10µM monomer of Rad52 or Rad52$^{\Delta C}$ with 10µM10µM Rad51). Formation of defined Rad51-bound Rad52 species is observed. In contrast, Rad52$^{\Delta C}$ displays more polydisperse behavior suggesting non-uniform complex formation with Rad51.

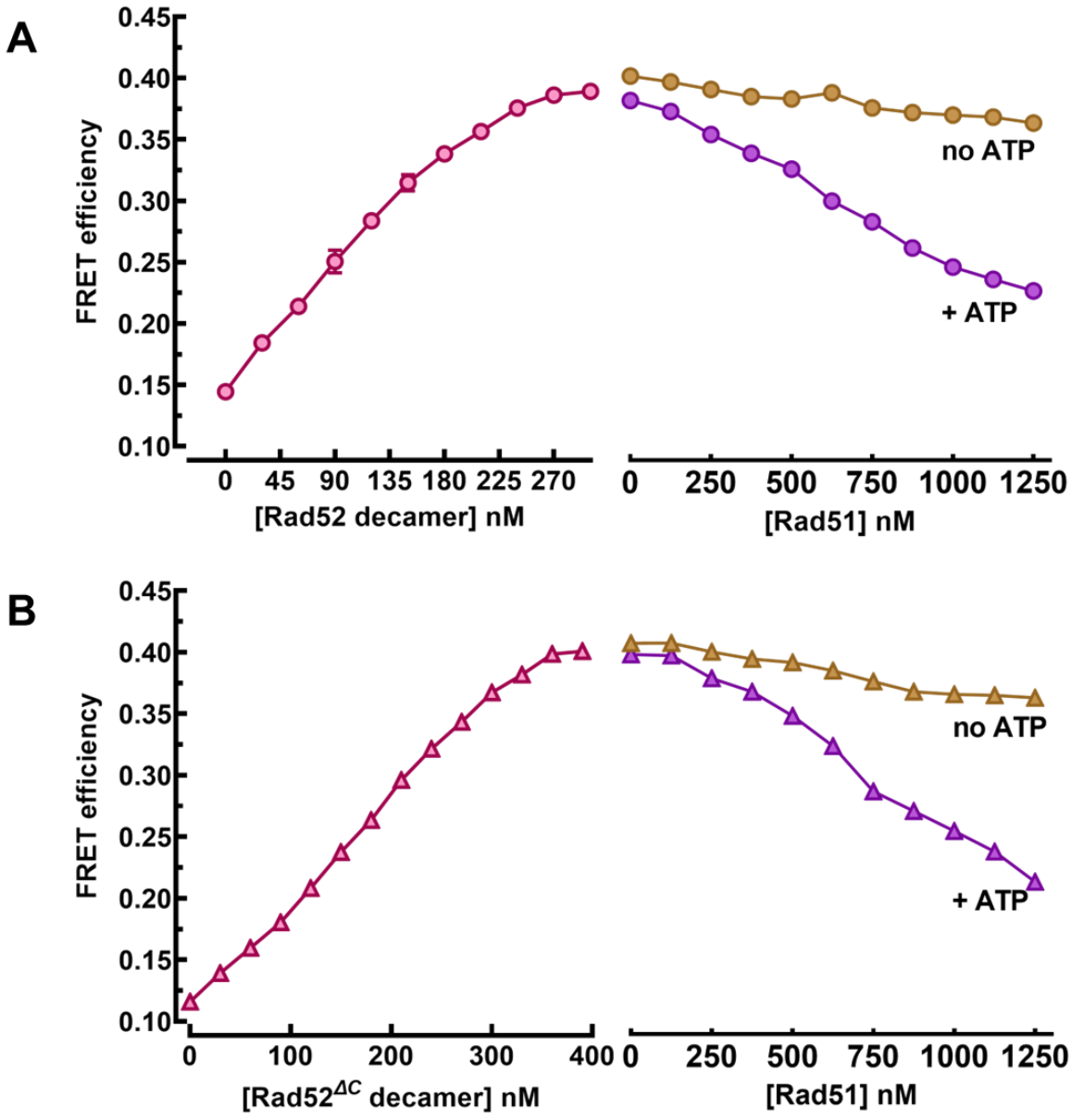

Supplementary Figure 21. Ensemble FRET measurements of Rad51-binding to Cy3-Cy5 end labeled $(dT)_{80}$ ssDNA. A) Rad52 or **B)** Rad52$^{\Delta C}$ were prebound to a Cy3-$(dT)_{80}$-Cy5 substrate and Rad51 was introduced in the absence or presence of ATP. Data shows that both Rad52 and Rad52$^{\Delta C}$-DNA complexes can be remodeled by Rad51 when sufficient time is provided to reach equilibrium.

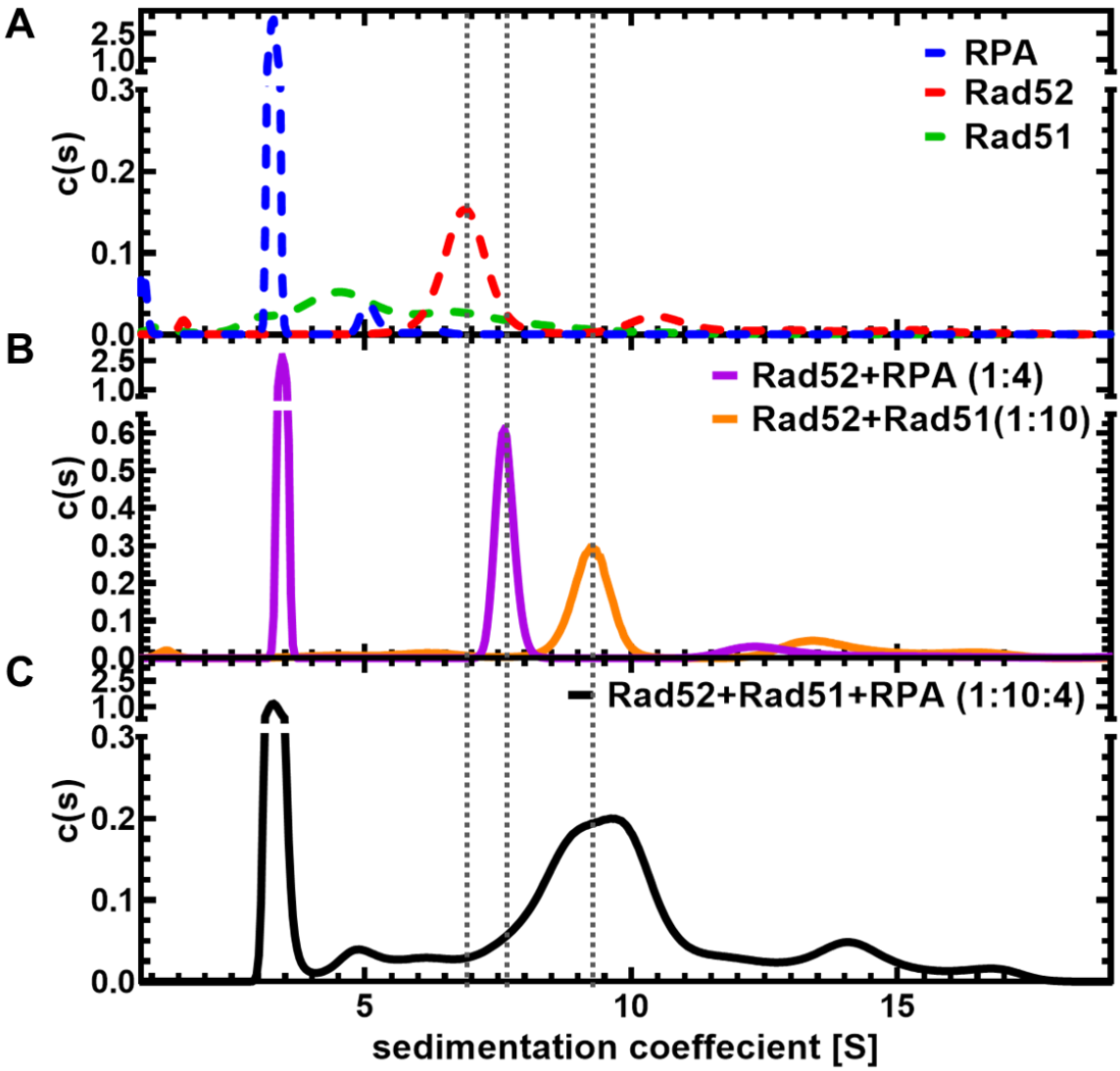

Supplementary Figure 22. RPA, Rad52, and Rad51 form a stable complex in the absence of ssDNA. Analytical ultracentrifugation sedimentation velocity analysis of RPA, Rad51, and Rad52 alone and in complex. **A)** Sedimentation profiles of RPA (4 μM), Rad52 (10 μM monomer), and Rad51 (10 μM). RPA is a single heterotrimer. Rad52 is predominantly a homodimer. Rad51 migrates as several polydisperse complexes. **B)** A complex between Rad52 (10 μM) and RPA (4 μM) or Rad51 (10 μM) shows formation of complexes. Even though 10 RPA binding sites are present in the Rad52 decamer, only a few RPA molecules are bound to the Rad52 ring. **C)** When all three proteins are mixed, a large species corresponding to RPA-Rad52-Rad51 are observed.

Supplementary Table I: Mass Photometer mass distribution

$(dT)_{84}$ kDa	**Rad52(n=8) kDa**	**Rad52 + $(dT)_{84}$ (n = 11)kDa**	**Rad52$^{\Delta C}$ (n=3) kDa**	**Rad52$^{\Delta C}$ + $(dT)_{84}$ (n=3)kDa**
63±19	72.9±14	87±26.	66±33.5	97
-	498.4 ±24	522.5±25	255±12	293±10
-	991.8±75	1078±68	517 ±29	606±17
-	1551(±9 8.99)	1562±37	782 ±46	931.5±29

** 1) Major peak (>85% of the population) is highlighted in bold*

2) All the different Rad52 and Rad52$^{\Delta C}$ peaks show ssDNA binding as can be seen in the systematic shift in the entire distribution

3) The $(dT)_{84}$ mass estimation is prone to lot of error because the actual mass of the ssDNA is 25,490.5 gm/mole which is at/below the detection limit of the of the scope

Supplementary Table 2: Velocity AUC c(s) numbers

Rad52	sw	Sw (20, w)	Mw (kDa)	Stokes Radius 20C (nm)	a/b (oblate)	a/b (prolate)	%
5μM	7.25	11.3	532	11.2	19.0	16.7	73.7
	11.0	17.1	991	13.8	19.0	16.7	04.4
	14.4	22.4	1484	15.8	19.0	16.7	02.2
10μM	7.14	11.1	521	11.2	19.0	16.8	81.8
	10.6	16.5	944	13.6	19.0	16.8	05.9
	13.9	21.7	1421	15.6	19.0	16.8	04.2
15μM	7.46	11.6	537	11.0	17.9	15.7	70.8
	13.11	20.4	1250	14.6	17.9	15.7	3.0

Supplementary Table 3. CryoEM data collection and model statistics

	Rad52 Apo
EMD	
PDB	
Data Collection and processing	
Magnification	150,000x
Voltage (kV)	200
Electron exposure (e^-/ $Å^2$)	50.7
Defocus range (μm)	-0.8 to -2.4
Nominal Pixel Size (Å)	0.94
Symmetry imposed	C10
Initial Particle images	701,962
Final Particle images	180,545
Map resolution (Å)	3.3/3.4/3.8
FSC threshold	0/0.143/0.5
Map resolution range (Å)	2.8 to 6.0
Refinement	
Model resolution (Å)	3.5
FSC threshold	0.143
Map sharpening B-factor (Å2)	
Model composition	
Chains	10
Non-hydrogen atoms	6930
Protein residues	890
Ligands	0
Water	0
Average B-factors ($Å^2$)	
Protein	71.88
Bond RMSD	
Bond lengths (Å)	0.003
Bond angles (°)	0.719
Validation	
MolProbity score	1.49
All-atom clash score	8.27
Ramachandran plot	
Favored (%)	97.87
Allowed (%)	2.18
Outliers (%)	0

Supplementary Table 4: Fluorescent or unlabeled DNA oligonucleotides used in various assays

Name	Sequence (5′ to 3′)	Comments
5′-FAM-$(dT)_{35}$	5'- /56-FAM/TTT TTT TTT TTT TTT TTT TTT TTT TTT TTT TTT TT -3'	Fluorescence Anisotropy
5′-FAM-$(dT)_{70}$	5'- /56-FAM/TTT TTT TTT TTT TTT TTT TTT TTT TTT TTT TTT TTT TTT TTT TTT TTT TTT TTT TTT TTT TTT T -3'	Fluorescence Anisotropy
5′-FAM-32bp-duplex	5'-/56-FAM/CGA ATG TAA CCA TCG TTG GTC GGC AGC AGG GC -3'	5′-FAM labelled oligo (sequence shown on the left) was hybridized with an unlabeled complementary strand to form a 32 base paired duplex for Rad52 binding experiments
$(dT)_{20}$	5'- TTT TTT TTT TTT TTT TTT TT -3'	Trp quenching
$(dT)_{30}$	5'- TTT TTT TTT TTT TTT TTT TTT TTT TTT TTT -3'	Trp quenching
$(dT)_{45}$	5'- TTT TTT TTT TTT TTT TTT TTT TTT TTT TTT TTT TTT TTT TTT TTT TTT -3'	Trp quenching
$(dT)_{60}$	5'- TTT TTT TTT TTT TTT TTT TTT TTT TTT TTT TTT TTT TTT TTT TTT TTT TTT TTT TTT -3'	Trp quenching
$(dT)_{84}$	5'- TTT TTT TTT TTT TTT TTT TTT TTT TTT TTT TTT TTT TTT TTT TTT TTT TTT TTT TTT TTT TTT TTT TTT -3'	Trp quenching, Mass Photometry
$(dT)_{97}$	5'- TTT TTT TTT TTT TTT TTT TTT TTT TTT TTT TTT TTT TTT TTT TTT TTT TTT TTT TTT TTT TTT TTT TTT TTT TTT TTT T -3'	Cryo-EM substrate, AUC
poly(dT)	-	Mean oligo length is 200 bases
5′-Cy5-$(dT)_{45}$-Cy3-3′	5'- /5Cy5/TTT TTT TTT TTT TTT TTT TTT TTT TTT TTT TTT TTT TTT TTT TTT /3Cy3Sp/ -3'	Fluorometer based ssDNA wrapping FRET assay
5′-Cy5-$(dT)_{60}$-Cy3-3′	5'- /5Cy5/TTT TTT TTT TTT TTT TTT TTT TTT TTT TTT TTT TTT TTT TTT TTT TTT TTT TTT TTT /3Cy3Sp/ -3'	Fluorometer based ssDNA wrapping FRET assay
5′-Cy5-$(dT)_{80}$-Cy3-3′	5'- /5Cy5/TTT TTT TTT TTT TTT TTT TTT TTT TTT TTT TTT TTT TTT TTT TTT TTT TTT TTT TTT TTT TTT TTT TTT TTT TTT TTT TT/3Cy3Sp/ -3'	Fluorometer based ssDNA wrapping FRET assay
5′-Cy5-$(dT)_{97}$-Cy3-3′	5'- /5Cy5/TTT TTT TTT TTT TTT TTT TTT TTT TTT TTT TTT TTT TTT TTT TTT TTT TTT TTT TTT TTT TTT TTT TTT TTT TTT TTT TTT TTT TTT TTT TTT T/3Cy3Sp/ -3'	Fluorometer based ssDNA wrapping FRET assay
5' -Cy5-18mer-Bio-3'	5' /5Cy5/GCC TCG CTG CCG TCG CCA/3Bio/ 3'	Biotin-ssDNA handle with 5'- Cy5
5' - 18mer-$(dT)_{40}$-Cy3-3'	5'- TGG CGA CGG CAG CGA GGC $(dT)_{40}$ /3Cy3Sp/ -3'	Partial duplex with $(dT)_{40}$ overhang
5' - 18mer-$(dT)_{60}$-Cy3-3'	5'- TGG CGA CGG CAG CGA GGC $(dT)_{60}$ /3Cy3Sp/ -3'	Partial duplex with $(dT)_{60}$ overhang
5' - 18mer-$(dT)_{80}$-Cy3-3'	5'- TGG CGA CGG CAG CGA GGC $(dT)_{80}$ /3Cy3Sp/ -3'	Partial duplex with $(dT)_{80}$ overhang

Supplementary Table 5: DNA Primers used for Rad52 mutagenesis

Name	Sequence (5′ to 3′)	Comments
$Rad52^{1-212}$ F	5'-ATATACATATGAATGAAATTATGGATATGGATGAG-3'	$Rad52^{\Delta C}$
$Rad52^{1-212}$ R	5'-GCAGTACTCGAGCTTCGTCGAGTCGGGATTG-3'	$Rad52^{\Delta C}$
$Rad52^{213-471}$ F	5'-ATATACATATGAACCTGGTGAAAATAGAAAATACAGTAAGTCG-3'	$Rad52^{\Delta N}$
$Rad52^{213-471}$ R	5'-GCAGTACTCGAGTCAAGTAGGCTTGCGTGCA-3'	$Rad52^{\Delta N}$
$Rad52^{293-471}$ F	5'-ATATACATATGGATCCCGTTGTAGCTAAGCAAAGCCC-3'	$Rad52^{\Delta N*}$
$Rad52^{293-471}$ R	5'-GCAGTACTCGAGTCAAGTAGGCTTGCGTGCATGCA-3'	$Rad52^{\Delta N*}$